catalysts

MDPI

Article

N-Doped TiO_2-Nb_2O_5 Sol–Gel Catalysts: Synthesis, Characterization, Adsorption Capacity, Photocatalytic and Antioxidant Activity

Maria E. K. Fuziki [1,*], Laura S. Ribas [2], Eduardo Abreu [1], Luciano Fernandes [3], Onélia A. A. dos Santos [1], Rodrigo Brackmann [4], Jose L. D. de Tuesta [5], Angelo M. Tusset [6] and Giane G. Lenzi [6]

1 Department of Chemical Engineering, State University of Maringá, Maringá 87020-900, Paraná, Brazil; eduardo_abreu@live.com (E.A.); oneliaandreo@hotmail.com (O.A.A.d.S.)
2 Department of Chemical Engineering, Federal University of Technology-Paraná, Doutor Washington Subtil Chueire St. 330, Ponta Grossa 84017-220, Paraná, Brazil; laurasantosribas@gmail.com
3 Department of Chemistry, Federal University of Technology-Paraná, Doutor Washington Subtil Chueire St. 330, Ponta Grossa 84017-220, Paraná, Brazil; lfernandes@utfpr.edu.br
4 Department of Chemistry, Federal University of Technology-Paraná, Via do Conhecimento, Km 1, Pato Branco 85503-390, Paraná, Brazil; rodrigobrackmann@utfpr.edu.br
5 Department of Chemical and Environmental Technology, Rey Juan Carlos University, 28933 Móstoles, Spain; joseluis.diaz@urjc.es
6 Department of Production Engineering, Federal University of Technology-Paraná, Doutor Washington Subtil Chueire St. 330, Ponta Grossa 84017-220, Paraná, Brazil; tusset@utfpr.edu.br (A.M.T.); gianeg@utfpr.edu.br (G.G.L.)
* Correspondence: mariafuziki@gmail.com

Abstract: TiO_2-based semiconductors are formidable photocatalysts for redox reaction applications. Although N-doped TiO_2-Nb_2O_5 catalysts have already been explored in the literature, studies on their antioxidant activity are scarce, and systematic investigations on the effects of synthesis parameters over a wide range of %Nb and NH_4OH concentrations are limited. In addition, the relationship between optimal pH and %Nb has not yet been adequately explored. In the present work, the sol–gel synthesis of N-doped TiO_2-Nb_2O_5 catalysts was optimized using a design of experiments approach focused on photocatalysis, adsorption, and antioxidant applications. The samples were characterized by TGA, SEM/EDS, XRD, PZC tests, photoacoustic spectroscopy, and N_2-adsorption/desorption experiments. The salicylic acid (SA) degradation tests and DPPH radical scavenging assays demonstrated the superior photocatalytic activity (up to 72.9% SA degradation in 30 min, pH 5) and antioxidant capacity (IC_{50} = 88.9 μg mL^{-1}) of pure TiO_2 compared to the N-doped TiO_2-Nb_2O_5 catalysts. The photocatalytic activity, however, proved to be intensely dependent on the pH and %Nb interaction, and at pH 3, the 25Nb-1N-400 catalyst promoted more significant SA degradation (59.9%) compared to pure TiO_2 (42.8%). In the methylene blue (MB) adsorption tests, the catalysts N-doped TiO_2-Nb_2O_5 showed removals at least seven times greater than TiO_2 catalysts without Nb.

Keywords: photocatalysis; advanced oxidation processes; antioxidant activity; salicylic acid; TiO_2; Nb_2O_5; design of experiments

Citation: Fuziki, M.E.K.; Ribas, L.S.; Abreu, E.; Fernandes, L.; dos Santos, O.A.A.; Brackmann, R.; de Tuesta, J.L.D.; Tusset, A.M.; Lenzi, G.G. N-Doped TiO_2-Nb_2O_5 Sol–Gel Catalysts: Synthesis, Characterization, Adsorption Capacity, Photocatalytic and Antioxidant Activity. *Catalysts* **2023**, *13*, 1233. https://doi.org/10.3390/catal13091233

Academic Editors: Xu Xiang, Pham Thi Huong and Minh Viet Nguyen

Received: 29 June 2023
Revised: 4 August 2023
Accepted: 21 August 2023
Published: 23 August 2023

1. Introduction

The control of water bodies' contamination and the search for more efficient technologies for the remediation of organic pollution in water have been the subject of several recent studies [1]. This type of pollution often involves the presence of dyes, pharmaceuticals, pesticides, pollutants of emerging concern, and so-called POPs (persistent organic pollutants), which may be very harmful to human life and aquatic ecosystems [1–4]. Advanced

oxidative processes (AOP) have been widely explored for the degradation of organic contaminants, mainly photocatalytic processes [5,6]. Photocatalysis is based on the formation of photogenerated electron/hole pairs, which can react directly with organic molecules and even completely mineralize them [5]. The strong dependency of these processes on the catalyst characteristics has motivated several efforts focused on photocatalyst improvement [7,8].

Titanium dioxide (TiO_2) is the most used photocatalyst, standing out for its chemical stability, low band gap (3.2 eV), photocatalytic activity under UV light, low toxicity, and environmentally benign characteristics [8–11]. Nevertheless, in the last decades, niobium pentoxide (Nb_2O_5) has stood out as an n-type semiconductor with a low band gap (3.4 eV) that may be applied as an alternative photocatalyst. While TiO_2 forms hydrocolloids in water and has increased hydrophilicity under UV radiation [9,12], Nb_2O_5 forms hydrocolloids of low stability in water, facilitating its separation [9,13,14]. About 98% of the world's niobium reserves are located in Brazilian territory, and 90% of all niobium sold worldwide comes from Brazil, followed by Canada and Australia [15].

Many efforts have recently been made in semiconductors' doping, mixed oxides synthesis, and heterojunction formation technologies to improve photocatalytic activity in organic pollutants degradation [5]. TiO_2-Nb_2O_5-based photocatalysts have already been applied in the degradation of compounds such as anti-inflammatories [16], dyes [17], herbicides [18], and cyanide oxidation [19]. Although pure titanium dioxide performs better than pure niobium pentoxide in some cases [20,21], studies indicate that the combination of these two semiconductors can bring benefits, such as increased absorption of visible light radiation, considerable improvement in the photocatalytic activity of TiO_2 [22,23], increased surface acidity of the catalysts, [23], greater sensitivity of the composite to UV radiation [18], and better charge separation in the heterojunction [24].

Previous studies on the TiO_2-Nb_2O_5 combination have not yet exhausted the investigation regarding the variation in the Ti/Nb proportions. Sacco et al., for example, prepared Pt–TiO_2–Nb_2O_5 by simply mixing the oxides in isopropanol at a fixed 1:1 ratio and calcining it at 650 °C [16]. Rafael et al. assessed the effects of Nb_2O_5 doping with small percentages of Ti (0.5–5.0%) in dyes degradation, reporting increased discoloration percentage as the Ti content increased [17]. Ferrari-Lima et al. carried out a fascinating study regarding the application of an N-doped TiO_2-Nb_2O_5 catalyst to the photocatalytic degradation of aromatic compounds, obtaining promising results for the N-doped Ti-Nb catalyst calcined at 500 °C. N-doping was performed by the addition of NH_4OH during the sol–gel synthesis. The work, however, was restricted to the study of the 50%TiO_2/50%Nb_2O_5 composition without evaluating the effect of the percentages of each phase [25]. Sedneva et al. studied the effects of %Nb (0.35% to 65%) and calcination temperature (80 to 1150 °C) on photoactivity, phase composition, and crystallite size. However, no assessment was made regarding the effect of solution pH on the catalyst performance [26]. There is a significant lack of studies addressing the impacts of pH variation on N-doped TiO_2-Nb_2O_5 catalysts' performance. Many relevant works on the Ti-Nb combination reported in the literature [22,25–30] did not discuss the effect of pH on the photocatalytic activity of the oxides. However, it is known that the pH directly affects the surface charges of the catalyst and the potential of the valence and conduction bands [31–33].

In this context, the present work proposes a systematic study of the TiO_2-Nb_2O_5 combination applied to salicylic acid degradation, considering a wide range of Ti:Nb ratios combined with the effect of the synthesis conditions and solution pH. It uses experimental design methodologies focused on optimizing %Nb and other synthesis and experimental parameters to improve the photocatalytic activity of the synthesized materials and statistically confirm the significance of the observed effects. A radical quenching study was conducted to understand better the main routes involved in the photocatalytic degradation process. As a differential, the present study focused on evaluating whether the addition of Nb favors the photocatalytic activity of the material in different pH conditions, considering not only the effects of pH on the catalysts' PZC but, mainly the impact of pH variation

on the potentials of the valence and conduction bands of the oxides, given that previous works on N-doped TiO_2-Nb_2O_5 catalysts [22,25–30] have not addressed this topic in depth.

Salicylic acid (SA) is an emerging pollutant generally found in higher concentrations in wastewater treatment plants [34] and sewage sludge [35]. This compound is also frequently used as a model pollutant for studying photocatalytic processes [36–38], mainly replacing dyes [39]. For this reason, SA was chosen as a model pollutant for evaluating the synthesized photocatalysts.

Recently, the number of studies concerning the antioxidant activity of photocatalysts has grown, with a view to reducing food oxidation or neutralizing the harmful effects of free radicals on cells [40–43]. To the best of the authors' knowledge, no investigation has been carried out on the antioxidant activity of N-doped TiO_2-Nb_2O_5 semiconductors. In this context, the antioxidant activity of N-doping TiO_2-Nb_2O_5 catalysts was studied in the present work using DPPH scavenging tests. As for the adsorption capacity of the catalysts, this was also evaluated by methylene blue (MB) adsorption tests, given that the MB molecule is already widely used in adsorption and photocatalysis studies [14,23,44–47].

2. Results and Discussion

2.1. Characterization Results

All synthesized catalysts were visually very similar, as a fine white powder. The SEM images (Figure 1) revealed a very rough and irregular microscopic surface, like tiny particles deposited over larger ones, as described by [25]. EDS spectra confirmed the presence of Nb in the catalyst in a mass percentage close to the theoretical Nb content.

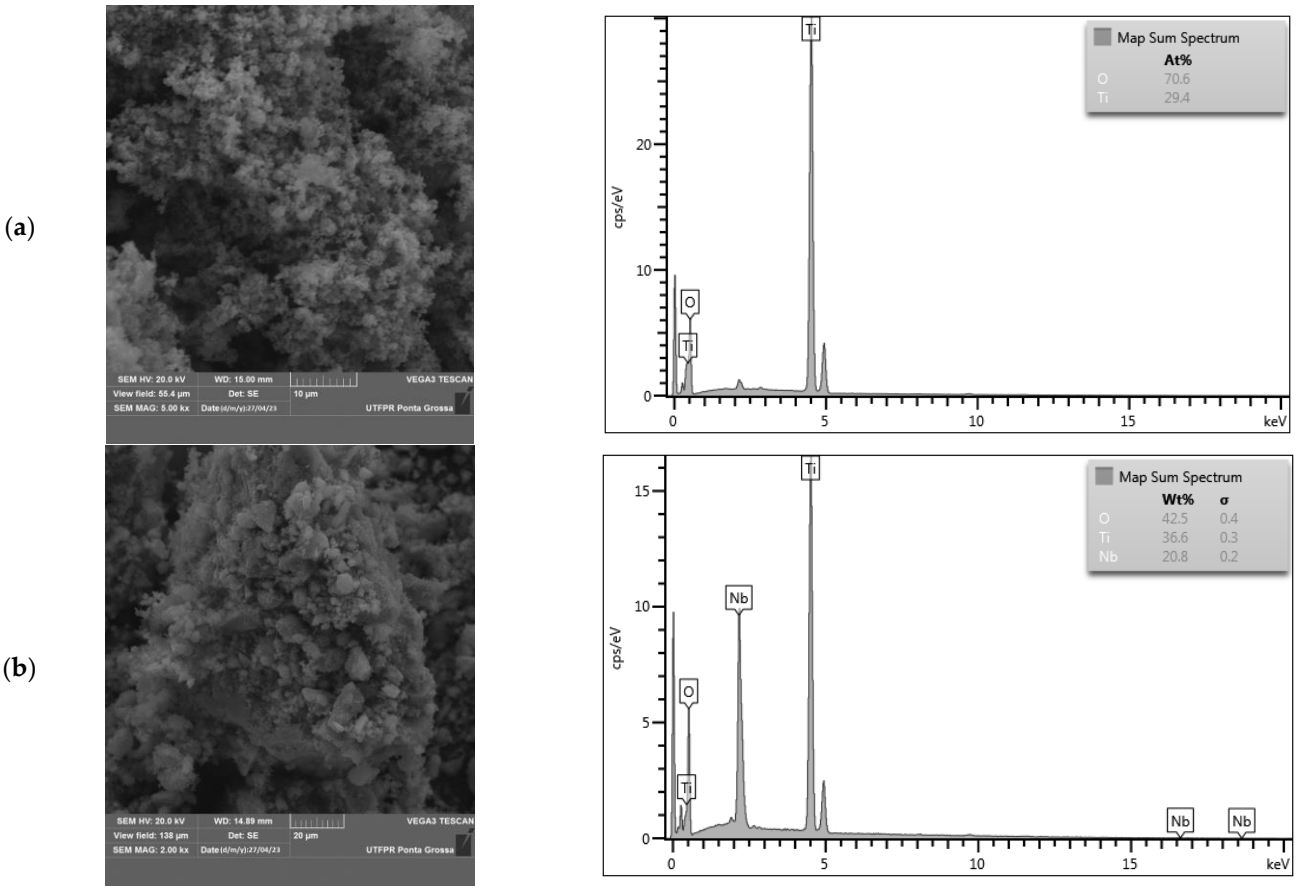

Figure 1. SEM/EDS results of (**a**) TiO_2, 0 mol of NH_4OH, 400 °C; (**b**) 25%, 1 mol of NH_4OH, 400 °C.

The TGA indicated close to 30% mass loss by heating the samples to 400 °C (Figure S1 in Supplementary Materials). After calcination at 400 °C, most of the catalysts became crystalline, as shown in Figure 2. According to the X-ray diffractograms, pure TiO_2 calcined

at 400 °C (0Nb-0N-400) was composed predominately by anatase phase (PDF#71-1167) and a small fraction of rutile (PDF#78-1510) (Figure 2h, peak around 27°). N-doping seems to have prevented rutile formation (Figure 2h) [25] and caused a slight displacement of peaks (Figure 2g,h). As for the pure Nb_2O_5 calcined at 400 °C (Figure 2a,b), minimal differences were observed in the diffractograms of undoped and N-doped samples, being possible to detect the Nb_2O_5 pseudohexagonal phase (TT-Nb_2O_5, PDF#28-0317) in both diffractograms.

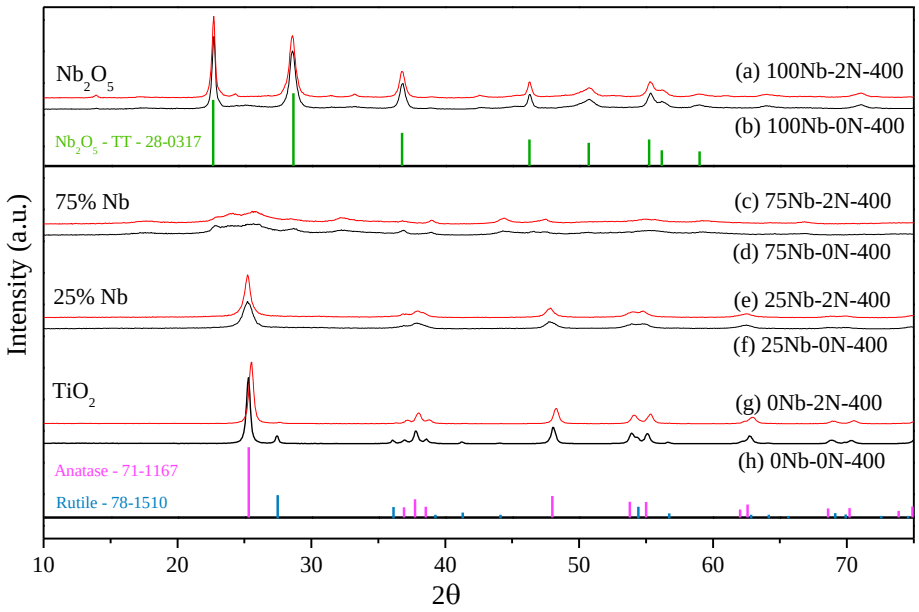

Figure 2. X-ray diffractograms of the catalysts calcined at 400 °C; black line—catalysts synthesized with no NH_4OH; red line—catalysts synthesized with NH_4OH:M = 2.

In Figure 2c–f, the crystallinity of the mixed oxides calcined at 400 °C decreased as the Nb content increased. The widening of anatase peaks in the 25%Nb samples (Figure 2e,f) is evident compared to the TiO_2 samples calcined at the same temperature. The presence of Nb^{+5} ions in the structure stresses the TiO_2 lattice, hindering the growth of crystallites and reducing the crystallinity of the sample, as observed by [27]. The Nb incorporation also contributed to preventing rutile formation. Silva et al. observed that Nb doping could postpone anatase–rutile transformation at almost 150 °C [48]. According to Castro et al., this postponing effect of Nb addition can be observed even in samples calcined at higher temperatures, around 700 °C [49]. The 25Nb-0N-400 and 25Nb-2N-400 diffractograms did not evidence peaks associated with any niobium phase, while 75Nb-0N-400 and 75Nb-2N-400 catalysts proved to be amorphous, with no characteristic peaks (Figure 3c,d).

N-doping seems to have caused a modest increase in crystallinity in the sample 25Nb-2N-400 (Figure 2e), as confirmed by the crystallite sizes estimated for the 25%Nb catalysts (from 10.2 nm in the undoped sample to 16.1 nm in catalysts produced with NH_4OH, see Table 1). Raba et al. reported a similar result, stating that the synthesis catalyzed in an alkaline medium tends to increase crystallites [13]. However, the crystallite size of pure TiO_2 and Nb_2O_5 catalysts slightly decreased after N-doping.

Calcination at 800 °C strongly impacted the crystalline structure (Figure 3), causing a relevant increase in crystallinity in all samples, as confirmed by de crystallite size estimations (Table 1). The anatase phase was transformed into rutile (Figure 3g,h) in the TiO_2 catalyst, while the monoclinic phase (PDF#72-1121) was the main phase identified in the Nb_2O_5 sample (Figure 3a,b). In the present work, obtaining the Nb_2O_5 monoclinic phase at a relatively low temperature was possible compared to reports [50]. In the mixed oxide catalysts, two additional phases were detected: the $TiNb_2O_7$ phase (PDF#39-1407) in the 25%Nb samples (Figure 3e,f) and the $Ti_2Nb_{10}O_{29}$ phase (PDF#40-0039) in the 75%Nb catalysts (Figure 3c,d).

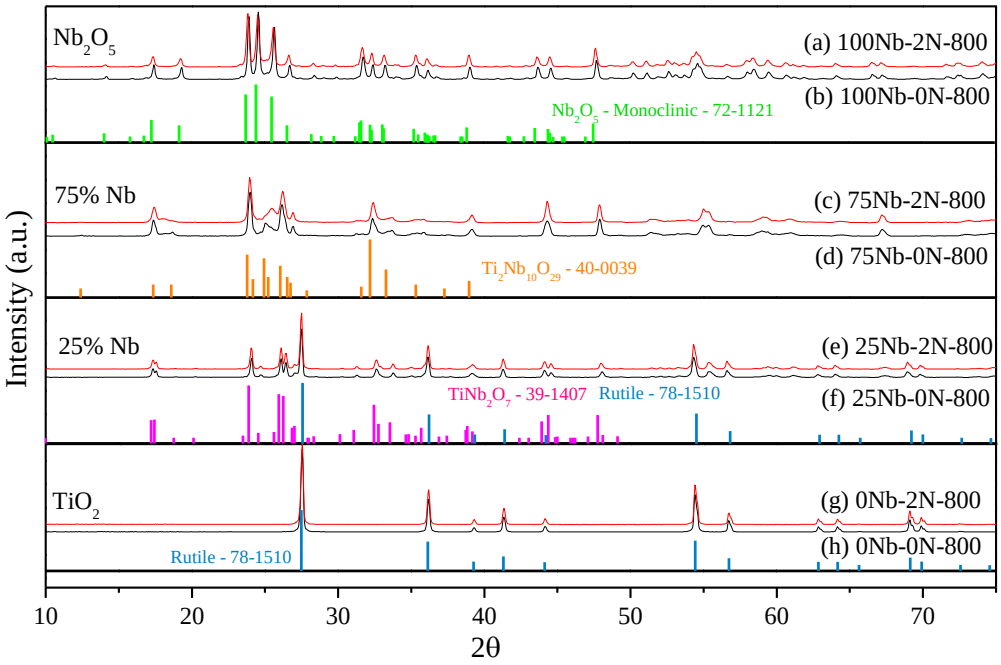

Figure 3. X-ray diffractograms of the catalysts calcined at 800 °C; black line—catalysts synthesized with no NH_4OH; red line—catalysts synthesized with NH_4OH:M = 2.

Table 1. Catalysts' textural properties, identified phases, percentages, and crystallite size.

Catalyst	S_{BET} $m^2\ g^{-1}$	$S_{langmuir}$ $m^2\ g^{-1}$	V_{total} $mm^3\ g^{-1}$	Identified Phases	d_m (nm)
0Nb-0N-400	18	154	45	Anatase	27.0
				Rutile	41.3
0Nb-2N-400	18	229	49	Anatase	23.5
25Nb-0N-400	86	395	132	Anatase	10.2
25Nb-2N-400	86	601	178	Anatase	16.1
75Nb-0N-400	29	230	71	Amorphous	-
75Nb-2N-400	27	276	78	Amorphous	-
100Nb-0N-400	22	260	76	TT-Nb_2O_5	32.5
100Nb-2N-400	20	215	72	TT-Nb_2O_5	32.1
0Nb-0N-800	4	14	5	Rutile	96.1
0Nb-2N-800	3	19	6	Rutile	99.4
25Nb-0N-800	0	0	0	Rutile	77.3
				$TiNb_2O_7$	61.8
25Nb-2N-800	0	0	0	Rutile	79.6
				$TiNb_2O_7$	92.9
75Nb-0N-800	0	0	0	$TiNb_2O_7$	-
				$Ti_2Nb_{10}O_{29}$	-
75Nb-2N-800	0	0	0	$TiNb_2O_7$	-
				$Ti_2Nb_{10}O_{29}$	-
100Nb-0N-800	0	0	0	Monoclinic Nb_2O_5	60.57
100Nb-2N-800	2	8	2	Monoclinic Nb_2O_5	54.63

The formation of a pure TiO_2 phase (rutile) and a mixed phase ($TiNb_2O_7$) in the 25%Nb catalysts suggests that Nb is not homogeneously dispersed in the sample. According to [51], niobium tends to segregate on the surface of Nb-doped TiO_2 (0.18 to 0.018% atom Nb) under oxidizing atmospheres. Based on this, Silva et al. stated that $TiNb_2O_7$ formation at 800 °C indicates niobium segregation in the catalyst surface [49]. Silva et al. estimated 2 mol% Nb_2O_5 as the maximum limit from which a second phase is formed, probably with the occurrence of surface segregation [48]. The second phase could not be visualized in the sample calcined at 400 °C, probably due to the low crystallinity [49].

The thermal treatment at 800 °C caused a drastic decrease in the specific surface area and pore volume (Table 1). The combination of Ti and Nb and calcination at 400 °C produced oxides with a higher specific area ($S_{BET,25Nb\text{-}0N\text{-}400}$ = 86 m^2 g^{-1}, and $S_{BET,75Nb\text{-}0N\text{-}400}$ = 29 m^2 g^{-1}) than pure oxides ($S_{BET,0Nb\text{-}0N\text{-}400}$ = 18 m^2 g^{-1} for TiO_2 and $S_{BET,100Nb\text{-}0N\text{-}400}$ = 22 m^2 g^{-1}). This evidences that Nb incorporation into titania favors an increase in the S_{BET}, producing S_{BET} values four times as high as synthesized TiO_2 specific area. This increase in surface area was expected, along with a decrease in surface energy and increased stability of nanoparticles [48]. Considering the area determined by the Langmuir model, it was possible to notice that, in general, the use of NH_4OH led to an increase in the specific surface area of the catalysts. The same behavior was not noticed in the specific area values determined by the BET model.

The analysis of the adsorption isotherms (Figure S3) indicated that the TiO_2 samples presented isotherms similar to type III, and the TiO_2 catalyst prepared with the addition of NH_4OH showed a slight H3 hysteresis loop. Vaizoğullar observed a similar type of isotherm for his MoS_2 photocatalyst, associating it with the unrestricted adsorption in multilayer and the H3 hysteresis with the presence of slit-like pores in the catalyst [52]. The undoped 25%Nb sample (Figure S3c) showed a characteristic type IV isotherm associated with mesoporous materials with pores larger than 4 nm [53,54]. The other samples showed isotherms with intermediate characteristics between these two.

The Rietveld refinement performed (Figure 4), based on the work of [55] on the TT-Nb_2O_5 phase, resulted in the structure represented in Figure 5a. The refinement of the 25% sample indicated an increase and slight distortion in the cell parameters of the anatase phase after Nb doping (Table 2) due to the difference in the ionic radius of Nb, evidencing Nb atoms incorporation into TiO_2 structure [48].

Table 2. Cell parameters obtained in Rietveld refinement.

χ2	Sample	Phase	a	b	c	Alfa	Beta	Gamma	Volume
1.271	0Nb-0N-400	anatase	3.784329	3.784329	9.511708	90	90	90	136.219
		rutile	4.59335	4.59335	2.959285	90	90	90	62.438
2.901	25Nb-0N-400	anatase	3.805582	3.805582	9.524768	90	90	90	137.942
5.244	100Nb-0N-400	TT-Nb_2O_5	6.221601	29.05318	3.926213	90	90	90	709.691

As for the optical properties of the catalysts, there was no significant variation in the band gap of the samples (Figure S4). Table 3 summarizes the estimated values for some catalysts calcined at 400 °C. Undoped and N-doped TiO_2 samples showed the lowest direct (3.04 eV) and indirect (2.93–2.94 eV) band gap energies. On the other hand, catalysts with 12.5 or 25% Nb showed a slightly higher band gap, closer to the values presented by Nb_2O_5 samples (3.11–3.14 eV). Nitrogen doping caused different effects on the band gap value depending on the %Nb: it was indifferent to TiO_2, causing an increase in the band gap for mixed oxides and a decrease for Nb_2O_5.

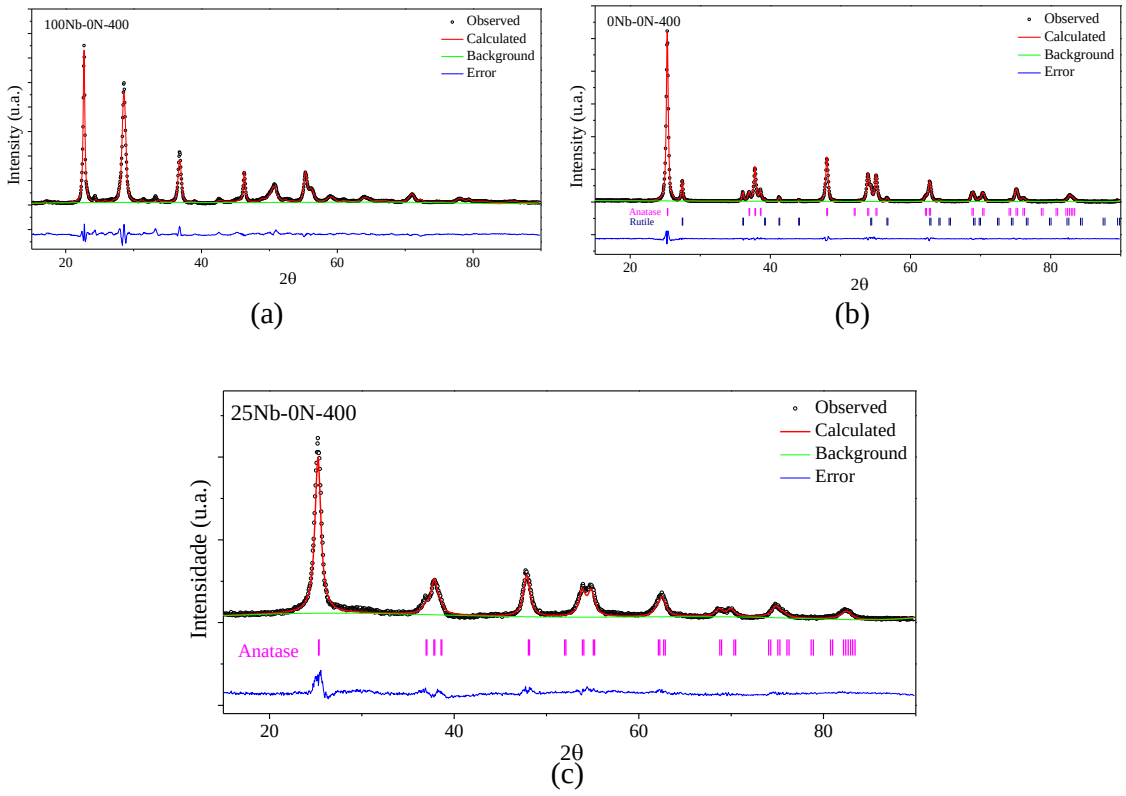

Figure 4. Rietveld refinement results. (**a**) 100Nb−0N−400; (**b**) 0Nb−0N−400; (**c**) 25Nb−0N−400.

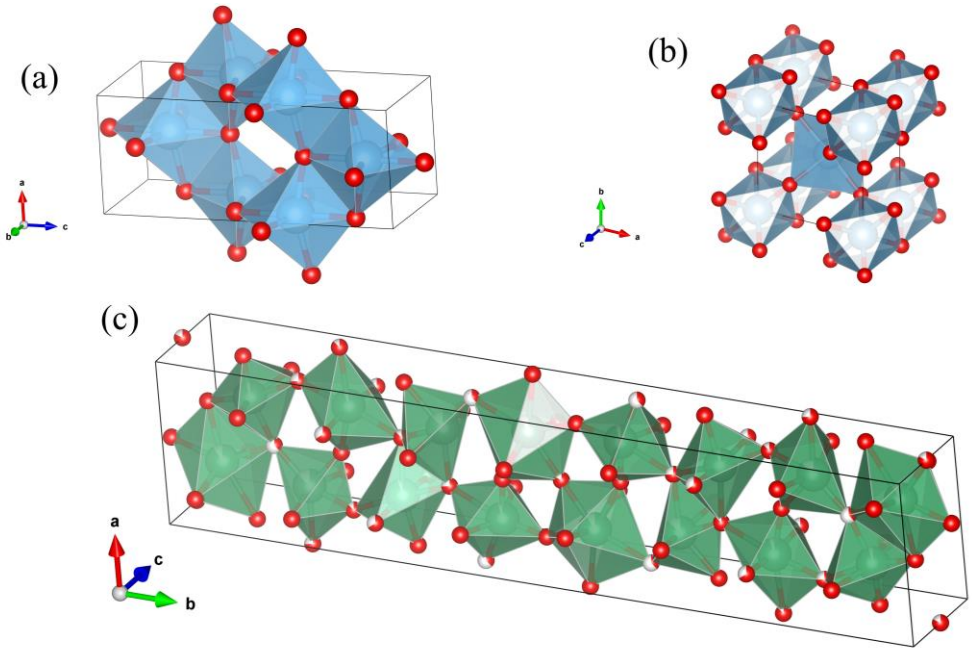

Figure 5. Phase structures obtained from Rietveld refinement results: (**a**) Anatase, (**b**) Rutile, (**c**) TT-Nb_2O_5 phases.

Table 3. Band gap values estimated for samples calcined at 400 °C.

	Band Gap Energy (E_g)	
Sample	**Direct**	**Indirect**
0Nb-0N-400	3.04	2.94
0Nb-1N-400	3.04	2.94
0Nb-2N-400	3.04	2.93
12.5Nb-0N-400	3.04	2.98
12.5Nb-1N-400	3.16	3.04
12.5Nb-2N-400	3.17	3.01
25Nb-0N-400	3.12	2.98
25Nb-1N-400	3.18	3.03
25Nb-2N-400	3.17	3.00
100Nb-0N-400	3.14	3.01
100Nb-2N-400	3.11	2.99

The band gap values observed in the present work are in accordance with literature reports. Kumari et al. calcined Nb_2O_5 samples at different temperatures and registered band gap values between 3.06 and 3.09 eV for the samples with an orthorhombic structure [50]. Rafael et al. synthesized catalysts with higher Nb_2O_5 content (95–99.5%) with band gap energies in the range from 3.10 and 3.35 eV [17], while Ücker obtained Nb_2O_5/TiO_2 catalysts with band gaps of 3.4 eV [29].

In the plots of photoacoustic signal vs. wavelength (Figure 6), two samples stand out: 0Nb-0N-400 and 25Nb-1-400. They presented the two most intense absorption bands in the graph, the 25Nb-1N-400 sample with a more intense and narrow absorption band and pure TiO_2 (0Nb-0N-400) with a broader absorption band, including the region between 400 and 420 nm.

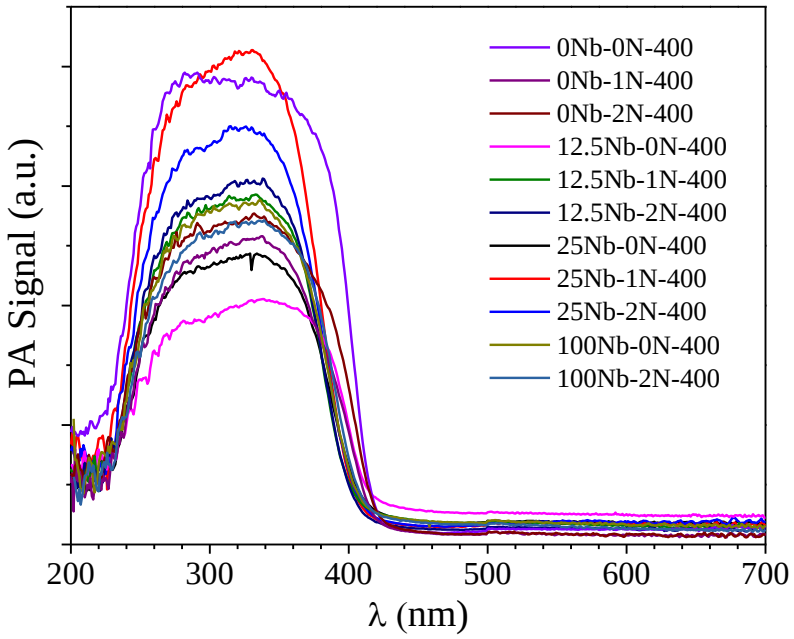

Figure 6. Photoacoustic signal vs. wavelength.

2.2. Photocatalytic Activity Tests

2.2.1. The 2^4-Factorial Design: Screening Tests

In the first set of experiments, the catalysts calcined at 800 °C presented the lowest removal percentages (Figure 7a). For 25%Nb catalysts, the probable cause for this behavior would be the complete conversion of anatase to rutile (Figure 3) and the drastic decrease in the specific surface area (Table 1) after calcination at 800 °C. Although combining anatase and rutile in optimal proportions is beneficial for the photocatalytic process, higher rutile contents reduce the catalyst performance due to the inferior photocatalytic activity of rutile [56]. Its lower activity is closely related to the decrease in specific surface area and increase in pore size, resulting in a limited number of available active sites [56].

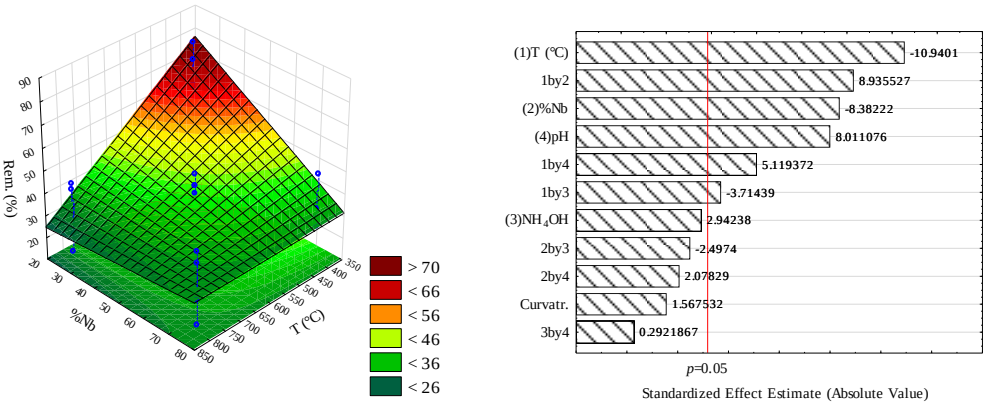

(**a**) (**b**)

Figure 7. Main results of the 2^4-factorial design: (**a**) Response surface in the function of %Nb and T_{calc}, pH = 5, NH_4OH:M = 1. Blue dots represent the experimental results (**b**) Pareto chart. Red line indicates $p = 0.05$.

Catalysts containing 75% of niobium, in turn, presented inferior results, regardless of the calcination temperature (Figure 7a), probably because they are amorphous at 400 °C, and, despite becoming crystalline at 800 °C, they suffered a drastic decrease in their specific surface area. Statistical analysis of results confirmed the strong effect of T_{calc} and %Nb on the photocatalytic activity. The effects estimate of the 2^4-factorial design indicated significant linear effects of the calcination temperature, niobium percentage, and pH (Figure 7b). The first two were negative, and the last positive, suggesting that decreased T_{calc} or %Nb and increased pH favors SA degradation. T_{calc} was the most significant effect, followed by T_{calc} interaction with %Nb and %Nb linear effect. Thus, T_{calc} and %Nb combined were the main determinants for the photocatalytic activity of the samples (Figure 7), given their direct impact on the critical properties of photocatalysts, such as crystalline structure (Figures 2 and 3), specific surface area (Table 1), charge separation, and superficial acidity, among others. Supplementary Materials reunites all the response surfaces, effect estimates, and the ANOVA table obtained for the 2^4-factorial design. Regarding the model adjustment, a linear model was fitted to the data (R^2 = 0.96405 e R^2adj = 0.91461) with no significant curvature or lack of fit (Table S1).

Significant interaction effects were detected involving T_{calc} and %Nb, and T_{calc} and pH. The response surface plotted as a function of %Nb and T_{calc} (Figure 7a) evidences the T_{calc}/%Nb interaction effect, given that decreasing %Nb potentializes the impact of calcination temperature.

N-doping presented a negative interaction effect with the calcination temperature, slightly improving the photocatalytic performance of catalysts calcined at 400 °C (Figure S1b).

Based on the analysis of the first block of experiments, it was clear that using catalysts with lower Nb content and calcined at lower temperatures radically favored the degradation of SA. Therefore, a new set of experiments was carried out using 0% to 25%Nb catalysts

in the same pH and NH_4OH:M range. As for the calcination temperature, despite its significant effect on the degradation of SA, increasing T_{calc} just caused a sharp reduction in the removal efficiency, even when considering interactions with other factors. The negative effect of the calcination temperature on the surface area also impacted this decision-making. That said, calcination temperature was excluded from the analysis, and T_{calc} was set at 400 °C, the lowest temperature required to remove organic residues from the catalyst (see TGA).

2.2.2. The 3^3-Factorial Design: Optimization

Additional tests were conducted in the second block of experiments using a 3^3-experimental design. The response surface obtained (R^2 = 0.93463 R^2_{adj} = 0.82765) was able to predict the experimental results with reasonable accuracy (Figure 8a). The model was significant with 95% confidence (p = 0.000386 < 0.05, $F_{Calculated}$ = 8.73 > $F_{Table,\ 0.05,18,11}$ = 2.67), while its lack of fit was not significant (p = 0.178122 > 0.05, $F_{Calculated}$ = 3.28874 < $F_{Table,\ 0.05,8,3}$ = 8.85). The ANOVA table is in the Supplementary Materials.

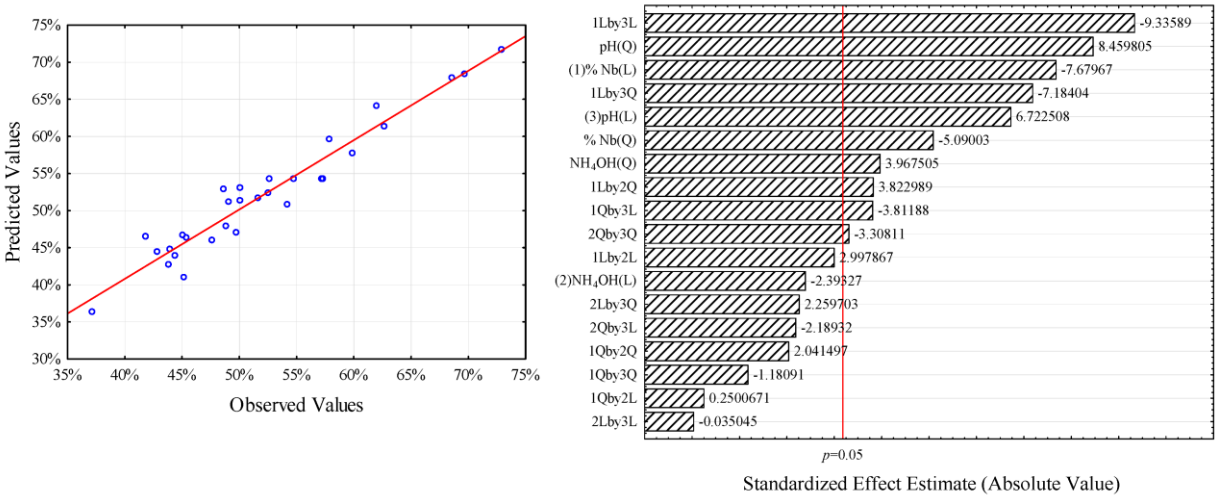

(**a**) (**b**)

Figure 8. (**a**) Removal model vs. values observed experimentally; (**b**) Pareto chart of the 3^3-experimental design, considering the linear (L), quadratic (Q), and interaction effects of the factors (1) %Nb, (2) NH_4OH:M, and (3) pH.

The effects estimates highlighted the relevance of the interaction between %Nb and pH (Figure 8b), followed by their respective linear and quadratic effects. The response surfaces at different pHs (Figure 9a–c) evidence that the %Nb effect is pH dependent. At pH 5 and 7, TiO_2 catalysts, notably 0Nb-0N-400, showed better results than mixed oxides, achieving 72.9% SA degradation in 30 min at pH 5. The better activity of the 0Nb-0N-400 catalyst may be related to the rutile phase in the samples, given that rutile in small amounts combined with the anatase phase can prevent the recombination of electron-hole pairs [57]. On the other hand, the samples containing Nb at pH 5 and 7, showed degradations between 44.4% and 57.3%, the latter being obtained by the catalyst 12.5Nb-1N-400 at pH 5.

At pH 3 (Figure 9a), the catalysts with higher %Nb present the best results. The photocatalyst 25Nb-1N-400 achieves 59.9% SA degradation compared to 42.8% degradation produced by 0Nb-0N-400. Surface plots in the function of pH and NH_4OH:M ratio (Figure 9d–f) also confirm this behavior. While TiO_2 catalysts' activity (Figure 9d) suffers a significant dependence on pH and is almost independent of N-doping, 25%Nb catalysts' performance (Figure 9f) depends on both pH and N-doping, with a maximum removal at pH 3 and NH_4OH:M ratio close to one.

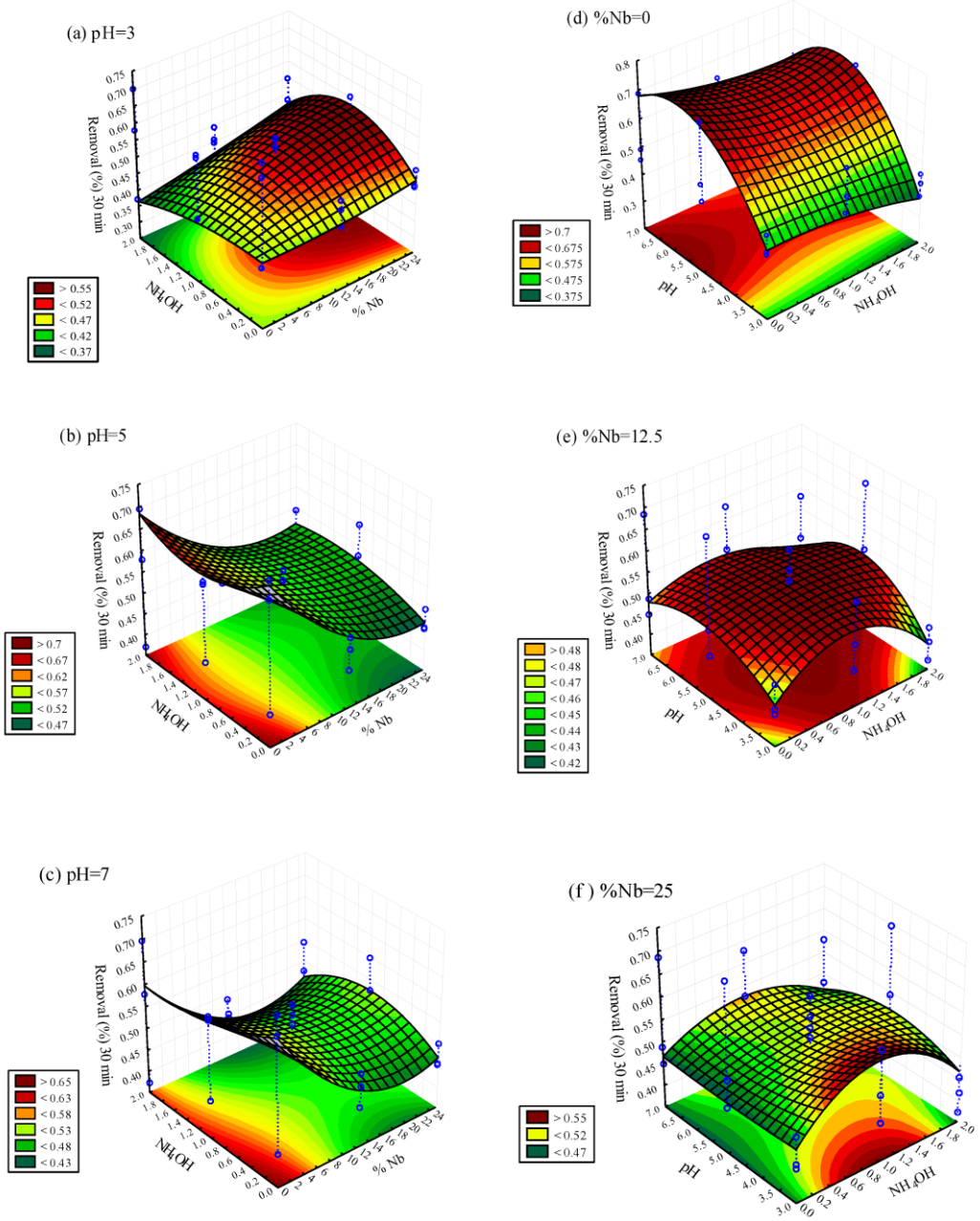

Figure 9. Response surface for SA degradation in 30 min, according to the 3^3 design. Response surfaces in the function of (**a**–**c**) %Nb and NH_4OH:M proportion, and (**d**–**f**) pH and NH_4OH:M proportion. Blue dots represent the experimental results.

Different reports have already been made in the literature regarding the effects of the Nb_2O_5 and TiO_2 combination. According to Rafael et al. [17], increasing Ti content in Ti-doped Nb_2O_5 catalyst promoted bromophenol blue degradation. It is important to emphasize that the tests were conducted at pH 5.5 [17]. On the other hand, Ahmad et al. (2008) observed that increasing Nb-doping in TiO_2 samples from 0.5 to 1.0 atom% improved the photocatalytic activity of the material in the degradation of 2-chlorophenol under sunlight [30], while Sacco et al. reported that Pt-TiO_2-Nb_2O_5 prepared with Ti:Nb = 1:1 presented a similar performance to Pt-TiO_2 in diclofenac degradation [16]. In the present case, as indicated in the response surfaces (Figure 9), only a minimal %Nb can be used without impact on the photocatalytic activity at pH 5 and 7. Although the TiO_2-Nb_2O_5 combination is beneficial for charge separation, the excessive increase in the Nb/Ti ratio (above 0.2) can lead to a decreased photocatalytic activity, given that an excessive number

of heterojunctions can act as recombination sites for electrons and holes [24]. In this sense, Shiraishi et al. affirmed that Nb^{+5} loading in TiO_2 is only beneficial at minimal concentrations, around 0.1%, due to the formation of NbO mononuclear species. Higher Nb^{+5} contents produced polynuclear Nb_2O_5 species, decreasing the activity of $Au/Nb^{5+}/TiO_2$ catalysts synthesized by the authors [28].

In contrast, Sedneva et al. [26] identified the optimal ratio in much higher niobium concentrations, between 15 and 30% Nb. The percentage of 25%Nb identified as optimal at pH 3 in the present work is within the range described by Sedneva [26], although the authors did not mention the effect of pH in their study. Many relevant works on the Ti-Nb combination [22,25–30] do not discuss the effect of pH on the photocatalytic activity of the oxides. Therefore, there is still much to be explored regarding this topic.

Given the electrostatic interactions between the organic molecule and the catalyst surface, it is necessary to ponder that the pH of the solution can directly affect the photocatalysis degradation efficiency of organic compounds like SA. Figure 10 shows the net specific surface proton excess vs. pH plots obtained from the potentiometric titration for samples 0Nb-0N-400 and 25Nb-1N-400. The point of zero charge determined for 0Nb-0N-400 was equal to 6.3, meaning that at pH 3 and 5 tests, the catalyst surface is predominantly positively charged ($pH < pH_{pcz}$), and the SA is negatively charged (pH > pKa = 2.98 [58]), a condition favorable for SA adsorption.

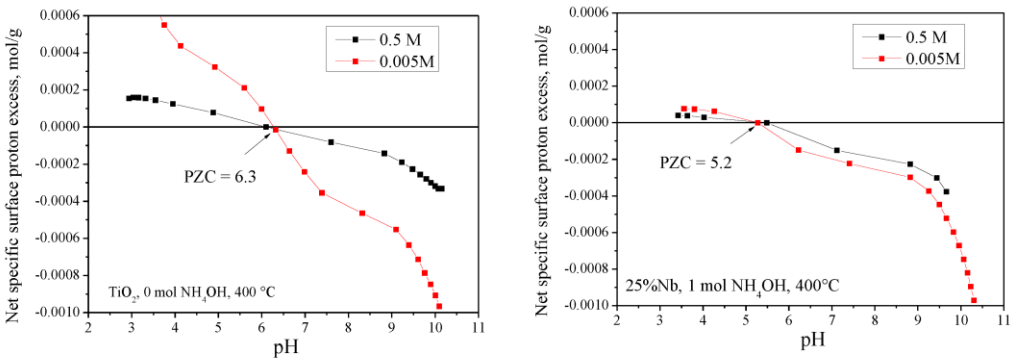

Figure 10. Net specific surface proton excess vs. pH functions of (**a**) 0Nb-0N-400 catalyst and (**b**) purified 25Nb-1N-400 catalyst.

The addition of Nb to TiO_2 led to a decrease in the pH_{pcz} of the catalyst (Figure 10b), restricting the pH range in which the electrostatic attraction between the negatively charged SA molecules (pH > pKa = 2.98 [58]) and the positively charged photocatalyst surface ($pH < pH_{pcz} = 5.2$) is more intense. Nonetheless, even when the surface of the 25Nb-1N-400 catalyst is positively charged ($pH < pH_{pcz}$), the values of net specific surface proton excess are lower than in the TiO_2 catalyst in the same condition.

Such observations, however, do not justify the results obtained from the photocatalytic degradation of SA, given that, based on the values indicated in Figure 10, the photocatalytic activity of the 0Nb-0N-400 catalyst is expected to increase at pH 3, due to the more intense interaction between the SA and the catalyst. Nevertheless, the opposite was obtained experimentally. Additional quenching tests were performed better to understand the SA degradation mechanism by N-doped TiO_2-Nb_2O_5 catalysts.

2.3. Quenching Tests: Contribution of Radicals

Photolysis tests (without catalyst addition) were initially performed at pH 3 and 7 (Figure 11a,d). The results obtained in the absence of scavengers (leftmost columns) confirmed the increase in photolytic degradation of SA when pH increases from 3 to 7, as previously reported [59]. Thus, in part, a more significant degradation of AS at pH 7 in photocatalytic tests is expected due to the considerable contribution of photolysis.

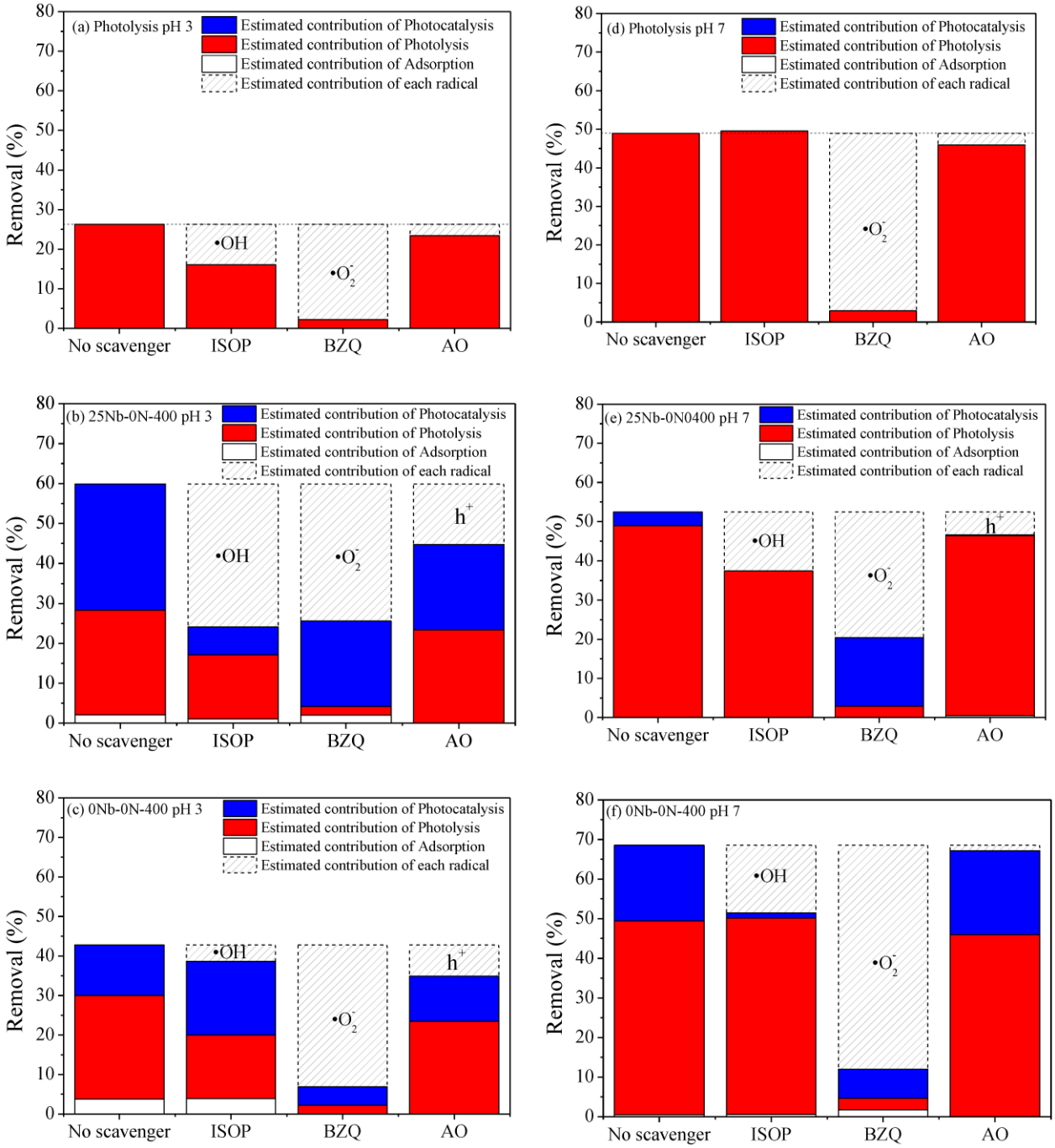

Figure 11. Removal percentages after 30 min of irradiation in quenching tests: (**a**) photolysis pH 3, (**d**) photolysis pH 7, photocatalysis using 25Nb-1N-400 catalyst in (**b**) pH 3 and (**e**) pH 7, and photocatalysis using 0Nb-0N-400 catalyst in (**c**) pH 3 and (**f**) pH 7.

The values of photolytic degradation obtained experimentally (red) were used to estimate the contribution of the photocatalysis process alone (blue), discounting photolysis. In addition, photolysis tests were performed in the presence of scavengers (ISOP, BZQ, and AO) to assess their effect on photolysis. AO, the hole (h^+) scavenger, did not significantly affect the photolytic degradation of SA, which was expected since no photogenerated holes participated in the photolysis reaction. The observed variation was minimal and could be attributed to experimental fluctuations. Isopropyl alcohol, a hydroxyl radical ($^{\bullet}$OH) scavenger, only affected photolysis at pH 3. The presence of benzoquinone, a

superoxide ($O_2^{\bullet -}$) radical scavenger, on the other hand, practically nullified photolysis both at pH 3 and pH 7.

In the photocatalytic tests with the 25Nb-1N-400 catalyst (Figure 11b,e) with no scavengers, discounting the estimated contributions of photolysis (red) and adsorption (white), it is evident how much the photocatalysis (blue) is relevant at pH 3, in contrast with pH 7. In tests with scavengers, the participation of hydroxyl radicals and holes is much more significant at pH 3 than at pH 7. The more significant participation of holes at pH 3 can be directly related to the better adsorption of AS molecules due to the surface charges of the catalyst. Even so, it is also necessary to consider that photogenerated holes contribute to hydroxyl radicals' formation.

On the other hand, for the 0Nb-0N-400 catalyst, the participation of hydroxyl radicals and the superoxide radical is much more relevant at pH 7. This seems to suggest that each catalyst favors a different degradation pathway. The reaction mechanism was analyzed from the perspective of the conduction band (*CB*) and valence band (*VB*) potentials to distinguish between the oxidation and reduction pathways. It is possible to estimate the band energy position using Equation (1) [60]:

$$E_{CB}^0 = \chi(S) - E^e - \frac{1}{2}E_g \quad (1)$$

In Equation (3), E_{CB}^0 is the conduction band edge position at the point of zero charge (PZC), E_g is the band gap energy of the semiconductor, and E^e corresponds to the energy of free electrons in the hydrogen scale (~4.5 eV) [60]. The term $\chi(S)$ is the electronegativity of the semiconductor, which can be calculated by the geometric mean of the electronegativity of the constituent atoms [60]:

$$\chi(S) = \sqrt[N]{\chi_1^n \chi_2^s \cdots \chi_{n-1}^p \chi_n^q} \quad (2)$$

where χ_n is the electronegativity of the constituent atom, n is the number of species, and N is the total number of atoms. Using Equation (2) and the electronegativity of Nb, Ti, and O atoms described by [61] and [60], the electronegativity of Nb_2O_5 and TiO_2 obtained were 6.23 eV and 5.83 eV, respectively. Applying these values and the E^e values obtained experimentally (Table 3) to Equation (1), E_{CB}^0 estimated for TiO_2 and Nb_2O_5 were $E_{CB,\ TiO_2}^0 = -0.13$ eV and $E_{CB,\ Nb_2O_5}^0 = 0.23$. Valence band energy position (E_{VB}^0) can be obtained from Equation (3) [17]:

$$E_{VB}^0 = E_{CB}^0 + E_g \quad (3)$$

From Equation (3), the obtained values were $E_{VB,\ TiO_2}^0 = 2.8$ and $E_{VB,\ Nb_2O_5}^0 = 3.24$. However, the position of the bands varies with pH, shifting negatively with increasing pH [31–33]. Considering that the values obtained for the positions of the valence and conduction bands refer to the pH_{pcz}, the following correction was made:

$$E_{CB} = E_{CB}^0 + 0.059(pH_{PCZ} - pH) \quad (4)$$

$$E_{VB} = E_{VB}^0 + 0.059(pH_{PCZ} - pH) \quad (5)$$

For N-doped Nb_2O_5, pH_{pzc} obtained experimentally was 6.0, while for pure TiO_2, the pH_{pzc} value was 6.3; for N-doped TiO_2, it was equal to 5.8. The corrected values are described in Figure 12.

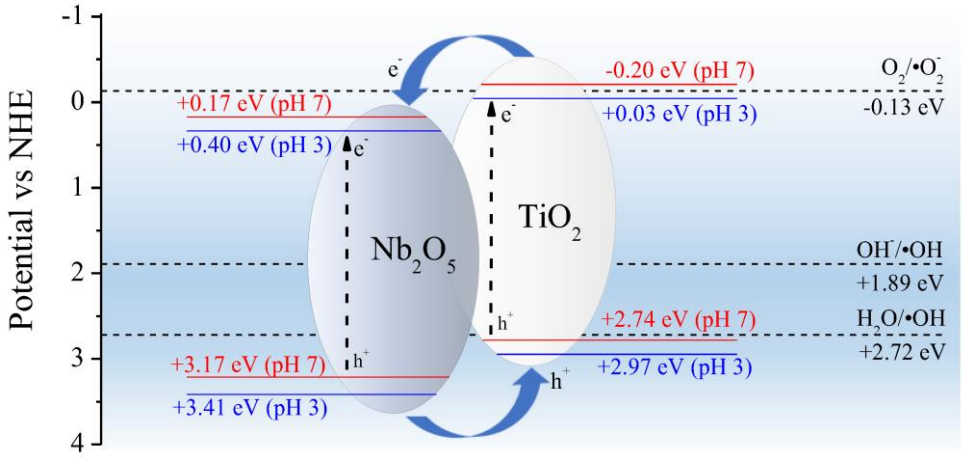

Figure 12. Schematic representation of the possible photocatalytic mechanism of N-doped TiO_2-Nb_2O_5 catalysts. Redox potentials from [62].

As can be seen in the comparison between the catalyst's band positions, photogenerated electrons in TiO_2 CB tend to migrate to Nb_2O_5 CB, while holes formed in Nb_2O_5 VB migrate to the VB of TiO_2, favoring charge separation in the heterojunction. As can be seen from the analysis of the radical's redox potentials [62], TiO_2 VB potential is more positive than $OH^-/^{\bullet}OH$ (+1.89 vs. NHE) and $H_2O/^{\bullet}OH$ (+2.72 vs. NHE) redox potentials [62], making hydroxyl radical generation thermodynamically favorable at both pHs. On the other hand, Nb_2O_5 CB potential is less negative than $O_2/O_2^{\bullet-}$ reduction potential, making its formation unfavorable at both pHs. This suggests that, in the case of the mixed oxide catalyst, the photocatalytic process takes place more by the oxidative route, with significant participation of photogenerated holes and hydroxyl radicals formed by the oxidative pathway.

For pure TiO_2, its conduction band potential at pH 7 (-0.17 eV) is slightly more negative than the $O_2/O_2^{\bullet-}$ reduction potential (−0.13 vs. NHE) [62], allowing the 0Nb-0N-400 catalyst to promote reduction pathway reactions at pH 7 (Figure 11f), with the contribution from both $O_2^{\bullet-}$ radical and $^{\bullet}OH$ radicals formed from $O_2^{\bullet-}$.

Reusability Tests

Reuse tests were carried out using the 25Nb-1N-400 catalyst, in 60 min lasting tests. At the end of each reuse cycle, a certain amount of SA stock solution was added to the medium to reestablish the initial concentration of the pollutant. The results obtained (Figure 13) indicated a reduction in the percentage of SA degradation, which became stabilized after the fourth cycle. In the last cycle, the catalyst reached only 73.9% of its degradation capacity presented in the first test. This reduction can be partly attributed to the accumulation of intermediaries formed by the degradation of the SA. The main reaction products of SA degradation by hydroxyl radicals have already been described in the literature as 2,3-dihydroxybenzoic acid, 2,5-dihydroxybenzoic acid, and catechol [63–67]. These compounds compete with SA for hydroxyl radicals, reducing the SA photocatalytic degradation rate.

Despite this reduction in degradation percentages, it can be said that the catalyst degradation capacity has been reasonably preserved, in view of the competition between SA and its by-products for the hydroxyl radicals formed. The reuse tests indicated the possibility of applying the synthesized catalysts in processes of longer duration, as well as in conditions where different organic compounds are simultaneously present.

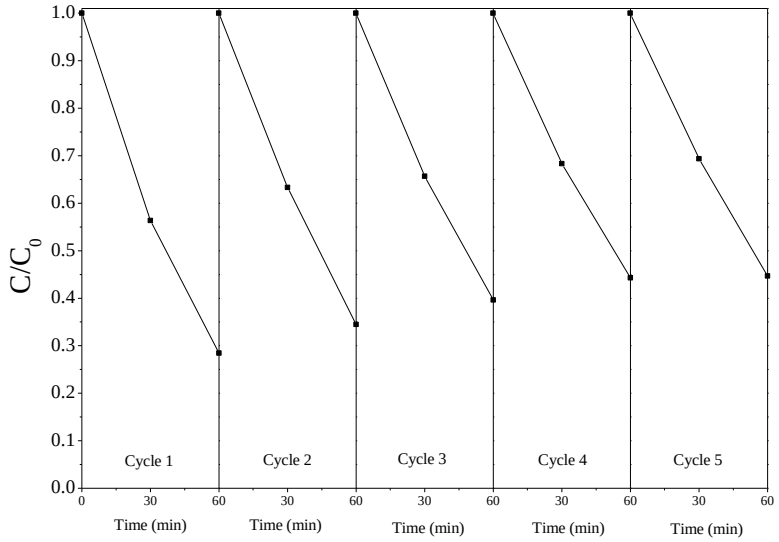

Figure 13. Reuse cycles of 25Nb-1N-400 catalyst applied to SA degradation. Each cycle duration was equal to 60 min, after which the cycle was restarted (vertical lines mark the cycles end/restart).

2.4. DPPH Assays: Antioxidant Capacity

In the DPPH scavenging tests (Figure 14), TiO_2 catalysts showed the highest inhibition percentages, with N-doping clearly showing a detrimental effect on their antioxidant activity. For the mixed TiO_2-Nb_2O_5 catalysts, on the contrary, the increase in the concentration of NH_4OH used in the synthesis favored the antioxidant activity, more pronounced in the catalysts with higher %Nb.

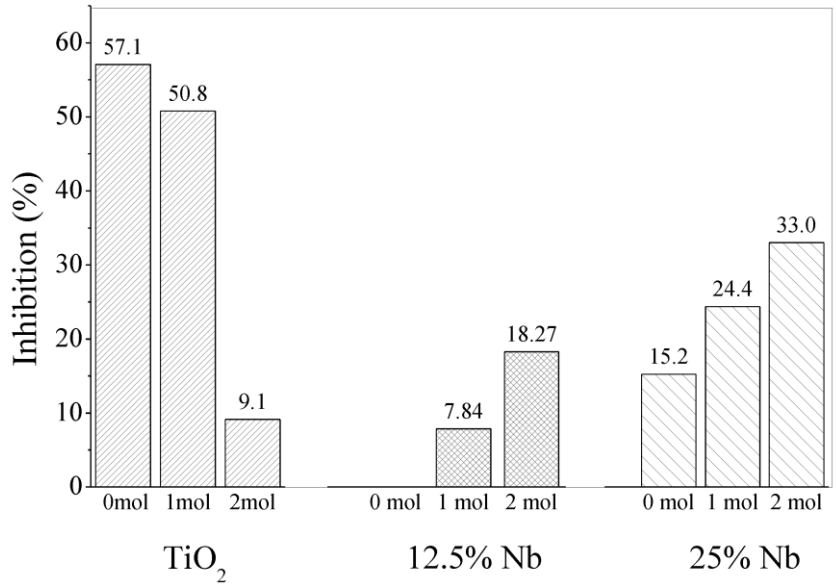

Figure 14. Comparison of DPPH scavenging percentages (inhibition) for different catalysts. Catalysts concentration in the tests: 1 mg mL^{-1}.

The catalyst with the best antioxidant activity was pure TiO_2 (0Nb-0N-400), with an estimated IC_{50} equal to 88.9 μg mL^{-1} (R^2 = 0.9932). However, even at considerably higher catalyst concentrations (up to 2 mg mL^{-1}), it was impossible to exceed 58.3% inhibition (Figure 15).

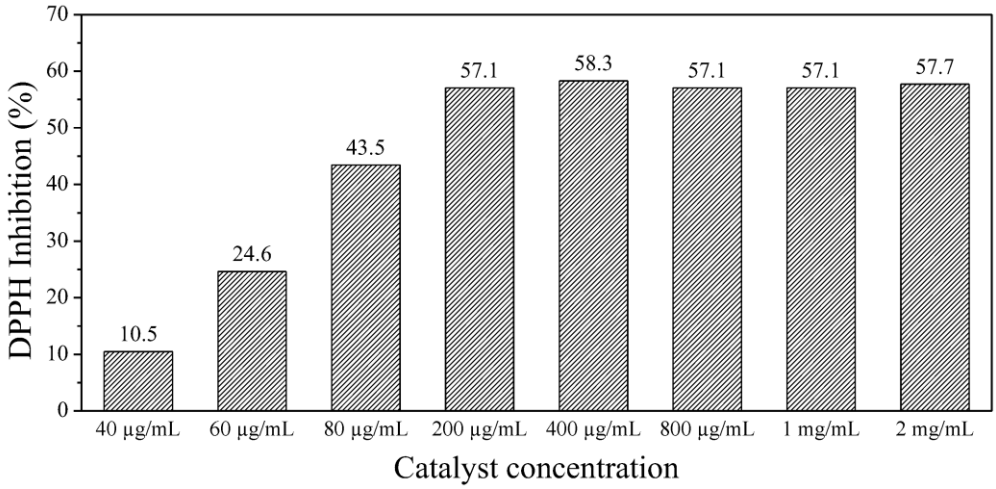

Figure 15. DPPH scavenging percentages for concentrations of 0Nb-0N-400 catalyst.

2.5. Methylene Blue Adsorption Tests

Although some catalysts have presented low specific surface areas, it is known that the adsorption capacity of a material does not depend exclusively on this property but also on the characteristics of its surface chemistry [45–47]. Thus, the following adsorption tests were carried out to provide an overview of their adsorption capacity and support future in-depth studies on their surface characteristics and applicability. Methylene blue was used as adsorbate given that it is a molecule already widely used in adsorption and photocatalysis studies [23,44], applied in evaluating adsorption and cation exchange capacity and surface area of clays [45–47], and is also recognized for its ability to interact with Nb_2O_5 acidic sites during adsorption [14]. The results of adsorption tests carried out according to the 3^2-experimental design are represented in Figure 13a. The response surface obtained was able to predict the experimental results with considerable accuracy. The ANOVA table is in the Supplementary Materials. The analysis of the effects confirmed the significance of all factors, highlighting the linear and quadratic effects of %Nb (Figure 16b).

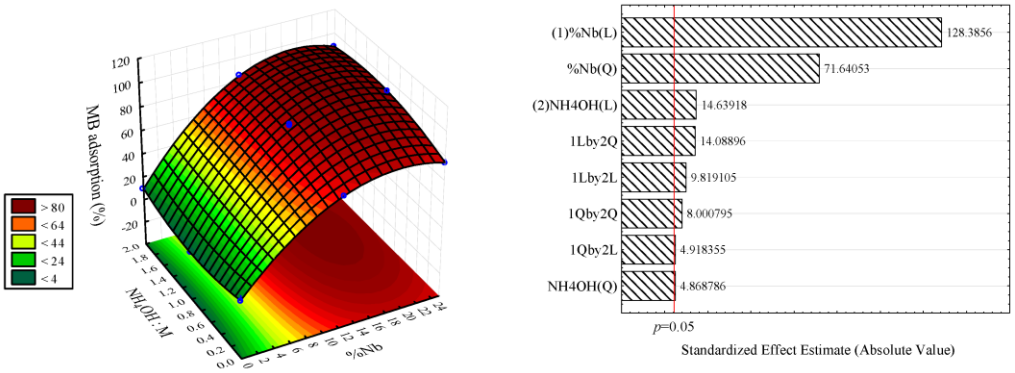

(**a**) (**b**)

Figure 16. Methylene blue adsorption results: (**a**) response surface for adsorption percentage and (**b**) Pareto chart. Blue dots represent the experimental results.

Catalysts containing Nb removed more significant percentages of MB, at least seven times higher than TiO_2 catalysts (Table 4). Likewise, the TiO_2-Nb_2O_5 catalysts also showed better results than Nb_2O_5.

Table 4. Methylene blue removal by adsorption.

Sample	MB Removal %
0Nb-0N-400	10.14
0Nb-1N-400	0.69
0Nb-2N-400	9.61
12.5Nb-0N-400	71.37
12.5Nb-1N-400	84.41
12.5Nb-2N-400	84.44
25Nb-0N-400	74.56
25Nb-1N-400	90.49
25Nb-2N-400	88.60
100Nb-0N-400	4.85
100Nb-2N-400	6.82

According to [68], the main mechanism of MB adsorption on Nb_2O_5 is the interaction between the dye molecules and Lewis and Bronsted acidic sites present on the catalyst. Metallic ions with reduced coordination on the oxide surface, like Nb^{+5}, can act as strong Lewis acidic sites [69] and interact with certain nucleophilic parts of methylene blue molecules, such as the electron pairs of nitrogen and sulfur, favoring adsorption [14]. In this sense, Ferraz et al. [23] reported that pure Nb_2O_5 showed a slightly higher MB removal capacity than the mixture of TiO_2-Nb_2O_5 oxides. Such results, however, differ from those currently observed (Table 4). Although the difference in the surface area of the catalysts (Table 1) may have contributed to these results, the fact that the mixed oxides showed a removal capacity between 7 and 9 times greater than that of TiO_2 and between 10 and 15 times greater than that of pure Nb_2O_5, compared to about a fourfold increase in surface area, suggests a strong influence of the surface characteristics of the materials.

Incorporating Nb in TiO_2 may increase surface acidity [22] and improve methylene blue adsorption [23]. MB adsorption results strongly suggest that the TiO_2-Nb_2O_5 combination contributed to an increased number of acidic sites on the catalyst surface [22], improving the adsorption of dye molecules. This fact is encouraging for dye-sensitization applications, given that the efficiency in this process is directly dependent on the efficiency of dye adsorption [70], making room for additional studies on the application of synthesized catalysts and their surface characteristics.

3. Materials and Methods

3.1. Chemicals

Acetylsalicylic acid (ASA, ≥98%-supplied by Biotec, São Paulo, Brazil), acetonitrile (HPLC—supplied by J.T. Barker, Ciudad de México, México), $NbCl_5$ (CBMM), titanium isopropoxide (Aldrich, São Paulo, Brazil), Tween 20 (Synth), isopropyl alcohol (ISOP, Êxodo científica, Sumaré, São Paulo, Brazil), p-benzoquinone (BZQ, Êxodo científica, Sumaré, São Paulo, Brazil), ammonium oxalate (AO, Êxodo científica, Sumaré, São Paulo, Brazil), and ammonium hydroxide (NH_4OH), phosphoric acid (Biotec), potassium phosphate monobasic (KH_2PO_4, Dinâmica, São Paulo, São Paulo, Brazil).

3.2. Synthesis of the Catalysts

The TiO_2-Nb_2O_5 catalysts were synthesized through a sol–gel methodology using different percentages of niobium (%Nb) in the total number of moles of metal ions (M = Ti +Nb). Titanium isopropoxide and $NbCl_5$ were used as precursors, and due to their high reactivity, both reagents were manipulated inside a glovebox containing an inert atmosphere (Ar).

$NbCl_5$ was dissolved into isopropanol and stirred until the solution became colorless. After this interval, Tween 20 and titanium isopropoxide were added to the mixture, con-

sidering the ratio of 30 g of Tween 20 for each mol of M (M = Ti^{4+} + Nb^{5+}) and respecting the %Nb determined by the experimental design. Finally, ultrapure water (15 mol of H_2O for each mol of M) mixed with different concentrations of NH_4OH (0, 1, or 2 mol for each mol of M) was added slowly, dropwise, to the mixture under intense agitation. The gel formed was left to age for 72 h at 25 °C. The precipitate obtained was filtered, washed with ultrapure water, dried at 60 °C overnight, and finally calcined at different temperatures (400 °C, 600 °C, or 800 °C) for five hours. The calcination process comprehended a heating rate of 1 °C min^{-1} and constant temperature steps every 100 °C, lasting 30 min.

The NH_4OH: M molar ratio and the calcination temperature used in the synthesis step were varied following the DoE (see Section 2.4). NH_4OH was used in the synthesis since it reduces gelation time [71] and affects drying and calcination steps of sol–gel synthesis [72]. The effect of NH_4OH addition was observed in the almost immediate formation of the gel in the present work, mainly in the case of Nb_2O_5, which presented the slowest gelation process. Regarding the use of Tween 20, reports indicated adding Tween 20 in the synthesis can help in shape control [73].

The catalysts' nomenclature was given by percentage of Nb, NH_4OH:M molar ratio, and calcination temperature; e.g., 0Nb-2N-800 represents TiO_2 catalyst (0% Nb), synthesized with 2 mols of NH_4OH per mol of Ti and calcined at 800 °C, while 25Nb-0N-400 corresponds to the catalyst containing 25% Nb, prepared with no addition of NH_4OH and calcined to 400 °C.

3.3. Characterization of the Photocatalysts

Rigaku MiniFlex 600 diffractometer (40 kV and 15 mA, Rigaku, Wilmington, MA, USA) was used to perform X-ray diffractometry (XRD) analysis of the catalysts, with Cu Kα radiation (k = 1.5406 Å), in step scan mode, with a step of 0.02° and a time per step of 2 s at a scanning interval of 2θ = 3–90°. The data were compared with the JCPDS (Joint Committee on Powder Diffraction Standards) database.

The thermogravimetric analyses were performed in TA Instruments equipment, model SDT Q-600 (Oxford, TESCAN, Saint Petersburg, Russia), with an analysis temperature range of 303 to 1073 K and a heating rate of 10 K min^{-1} in a nitrogen atmosphere and 100 mL min^{-1} flow. Surface characterizations were performed using scanning electron microscopy (SEM) and energy-dispersive X-ray spectroscopy (EDS) (Tescan Scanning Electron Microscope, Vega 3 LMU equipped with dispersive energy detector—EDS-Oxford, AZTec Energy X-Act).

The textural properties of the materials were determined from N_2 adsorption–desorption isotherms at -196 ºC. Firstly, samples were degasified using a micromeritics Smart Vacprep (Micromeritics Instrumen, Norcross, GA, USA), and secondly, N_2 adsorption–desorption isotherms were obtained using a Micromiretics TriStar II Plus adsorption analyzer. Surface areas and pore volume were determined using TriStar II Plus Version 3.03. The degassing of the samples was carried out based on the following heating program: up to 30 °C, at 10 °C/min and holding time of 3.3 min; up to 90 °C, at 5 °C/min and holding time of 30 min; and, finally, up to 150 °C, at 5 °C/min and holding time of 480 min.

The catalysts' point of zero charge (PZC) was determined using a potentiometric titration methodology [74]. The preparations for the analyzes included intense boiling of the water used in the solutions and purification of the analyzed catalysts by repeated washing steps with ultrapure water. A 50% NaOH stock solution was prepared and filtered to remove carbonates. For each titration, 50 mg of purified catalyst was suspended in 50 mL of electrolyte solution ($NaNO_3$, 0.005 M, and 0.5 M). Titration was then performed with NaOH and HNO_3 solutions, 0.1 M each, with additions of 50 µL, down-titration first, followed by up-titration. The pH of the suspension was recorded after reaching equilibrium. The correlation between pH and proton concentration was determined by a calibration curve, as described by [74]. The catalysts were also characterized by photoacoustic spectroscopy, as previously described in [75]. Direct and indirect band gap energies were estimated from the Tauc plot, as described in [76].

3.4. Desing of Experiments (DoE)

Initially, a 2^4-factorial design with 3 replicates of the central point was performed as a screening step to assess the most relevant factors affecting the N-doped TiO_2-Nb_2O_5 catalysts synthesis and photocatalytic performance. The factors and levels considered are described in Table 5. The %Nb (Equation (6)) represents the percentage of niobium in the total number of mols of metallic ions, M:

$$\%\text{Nb} = \frac{n_{Nb}}{n_M} \cdot 100 = \frac{n_{Nb}}{n_{Nb} + n_{Ti}} \cdot 100 \quad (6)$$

Table 5. Factors and levels considered in the 2^4-factorial design—Photocatalytic tests.

Level (Coded Variables)	%Nb (Molar)	NH_4OH:M (Molar Ratio)	T_{calc} (°C)	pH (Photocatalytic Tests)
−1	25	0	400	3
0	50	1	600	5
+1	75	2	800	7

Thus, %Nb = 0 represents pure TiO_2, and %Nb = 100 represents pure Nb_2O_5. NH_4OH:M is the molar ratio between ammonium hydroxide and M. The calcination temperature used as the final synthesis step is indicated by T_{calc} (°C). The fourth factor considered (Table 5) was the solution pH during the photocatalytic tests. The chosen pH range varied between 3 and 7, given that pH values close to 3 tend to maximize direct electron transfer processes involving SA, which are described as the main pathway responsible for its degradation [37].

Based on the results obtained in this initial screening step (2^4-factorial design), a new set of experiments was carried out, following a 3^3-factorial design, to optimize the photocatalytic activity of the catalysts. The factors and levels considered are described in Table 6.

Table 6. Factors and levels considered in the 3^3-factorial design—Photocatalytic tests.

Level (Coded Variables)	%Nb (Molar)	NH_4OH:M (Molar Ratio)	pH (Photocatalytic Tests)
−1	0	0	3
0	12.5	1	5
+1	25	2	7

The removal of methylene blue by adsorption was also studied following a 3^2-experimental design, with factors and levels indicated in Table 7.

Table 7. Factors and levels considered in the 3^2-factorial design—Adsorption tests.

Level (Coded Variables)	%Nb (Molar)	NH_4OH:M (Molar Ratio)
−1	0	0
0	12.5	1
+1	25	2

3.5. Photocatalytic Activity Tests

The photocatalytic activity of the synthesized catalyst was assessed in degradation tests of a model pollutant (salicylic acid or SA, C_0 = 50 mg L^{-1}). The solution was magnetically stirred, the reaction temperature was kept around 20 °C, and atmospheric air was continuously bubbled inside the reactor. The solution pH was adjusted to pH = 3, 5, or 7, using HCl and NaOH solutions, and the catalyst concentration in all tests was equal to

1.0 g L^{-1}, similar to that reported in other works [77–79]. In each experiment, the catalyst used and the pH value of the solution were determined according to the experimental design (see Section 2.4). Before every photocatalytic test, the suspension formed by the SA solution and the catalyst was kept in the dark for 60 min. After this interval, the Hg vapor lamp (250 W) without a bulb (34.10 mW cm^{-2}) was turned on, initiating the photocatalysis step. The suspension samples were collected during the experiment, centrifuged, and had their SA concentration determined by high-performance liquid chromatography.

3.6. High-Performance Liquid Chromatography (HPLC)

SA was quantified in the liquid samples by High-Performance Liquid Chromatography (HPLC, YL Clarity 9100, UV-VIS detector, monitoring at 210 nm, Young In Chromass Co., Gyeonggi-do, Coreia) using a C-18 column (Luna, 5 µm, 150 × 4.6 mm, Phenomenex). The mobile phase was 40/60 acetonitrile/phosphate buffer (pH = 2.8, 50 mM) at 1 mL min^{-1}, 30 °C. The methodology currently used was adapted from the work of [36], and the validation tests are described in detail in previous work [59].

3.7. Quenching Experiments

Quenching tests were performed to determine the main active species in SA degradation. Isopropyl alcohol (ISOP, 2 mM), benzoquinone (BZQ, 2 mM), and ammonium oxalate (AO, 2 mM) were used as $^{\bullet}OH$, $O_2^{\bullet-}$ and h^+ scavengers, respectively [80,81]. The experimental conditions were identical to those described in Section 3.5. Tests were carried out both in the absence (photolysis) and in the presence of the catalyst (photocatalysis) at two different pHs (3 and 7). The catalysts used were those with the most promising results in the experiments of the 3^3-factorial design.

3.8. DPPH Assays

The antioxidant activity of the catalysts was measured in DPPH radical inhibition assays [82,83]. In the tests, 1 mL of DPPH solution, 100 µM, was added to 3 mL of catalyst suspension, 1 mg mL^{-1}. After 30 min the dark, the suspension was centrifuged, and the sample was analyzed using a UV–Vis Spectrophotometer at 517 nm. The %DPPH inhibition was determined by Equation (7).

$$\%\text{DPPH inhibition} = \frac{\left(Abs_{blank} - Abs_{sample}\right)}{Abs_{blank}} \cdot 100 \quad (7)$$

3.9. Methylene Blue Adsorptions Tests

The adsorption capacity of the N-doped TiO_2-Nb_2O_5 catalysts was evaluated in equilibrium adsorption tests at pH3 using methylene blue as the model molecule. Each catalyst (1 g L^{-1}) remained in contact with 10 mL of MB solution (10 mg L^{-1}) for 24 h to reach equilibrium. At the end of this interval, samples were collected and centrifuged and had the MB concentration determined by UV–Vis Spectrometry at 665 nm. The results were evaluated using the 3^2-factorial design (Table 3, Section 2.4).

4. Conclusions

N-doped TiO_2-Nb_2O_5 photocatalysts were synthesized through a sol–gel methodology. The characterization of the catalysts indicated a strong effect of the calcination temperature on the properties of the catalysts, notably reducing the specific surface area and inducing phase transformation. These characteristics reflected directly on the photocatalytic activity of the catalysts, which decreased with increasing calcination temperature. In turn, the addition of Nb to TiO_2, in the molar ratio of 25:75 (Nb:Ti), was able to promote an increase of more than four times in the S_{BET} surface area, which went from around 18 m^2 g^{-1} to 86 m^2 g^{-1}.

According to the experimental design analysis, another relevant property considered was the niobium content (%Nb) of the catalysts, whose impact on photocatalytic activity

was strongly pH dependent. This interaction between pH and %Nb has not been addressed before in studies about N-doped TiO_2-Nb_2O_5 catalysts. The addition of Nb to TiO_2 proved favorable for the photocatalytic activity at pH 3, but negative at pH 5 and 7. Pure TiO_2 catalyst showed maximum SA removal at pH 5 (72.9%), which decreased to about 42.8% at pH 3 in 30 min of the photocatalytic test. In the same time interval, catalyst 25Nb-1N-400 promoted approximately 49.0% degradation at pH 5, which increased to 59.9% at pH 3, surpassing the performance of TiO_2 in the same condition. The results of the SA degradation tests indicated that the addition of Nb was only favorable in a specific pH range, close to three.

The solution pH was decisive for electrostatic interactions between surface/organic molecules and for the displacement of CB and VB potentials as the pH increased, directly impacting the formation of radicals and the degradation of organic molecules. The TiO_2 and Nb_2O_5 combination proved interesting for charge separation and oxidative pathway applications. Even so, future studies can be carried out to improve the applicability of the catalysts, in actual conditions of varied concentrations of pollutants, in different water matrices, with monitoring of the levels of toxicity, formation of by-products, degree of mineralization, and evaluating the use of different concentrations of catalysts.

In the antioxidant activity tests, catalysts without the addition of Nb were superior, with IC_{50} = 88.9 μg mL^{-1} for the catalyst 0Nb-0N-400. However, in the catalyst's comparison, N-doping improved the antioxidant activity, suggesting future studies optimizing the N content in TiO_2-Nb_2O_5 catalysts. On the other hand, the combination TiO_2-Nb_2O_5 excelled in methylene blue adsorption tests. The mixed oxides achieved a removal capacity between 7 and 9 times greater than that of TiO_2 and between 10 and 15 times greater than that of pure Nb_2O_5, compared to about a fourfold increase in surface area, suggesting a strong influence of the surface characteristics of the materials. According to literature reports, due to its structural characteristics, the MB molecule is adsorbed on catalysts by interactions with acidic sites of the surface. The adsorption results currently obtained open space for future in-depth studies on the surface characteristics of the synthesized catalysts.

Supplementary Materials: The following supporting information can be downloaded at https://www.mdpi.com/article/10.3390/catal13091233/s1, Figure S1. Thermogravimetric analysis results of samples; Figure S2. Response surfaces—linear model—for SA degradation (%) obtained in the four-factor experimental design (2^4); Figure S3. Adsorption isotherms of the samples calcined at 400 °C. Percentages of Ti:Nb. S = 0 mol of NH4OH. C = 2 mol of NH_4OH. Figure S4. Tauc plots for direct and indirect band gap estimations. Data obtained from photoacoustic spectroscopy analysis. Table S1. Effects estimates and model coefficients of the four-factor experimental design (2^4). Significant effects are highlighted in bold. Table S2. Effects estimates and model coefficients of the four-factor experimental design (2^4). Significant effects are highlighted in bold. Table S3. Photocatalytic results of the 3^3-experimental design. Table S4. ANOVA table of the 3^3-experimental design. Significant effects are highlighted in bold. Table S5. Effects Estimate. Variables as coded variables of the 3^3-experimental design. Significant effects are highlighted in bold. Table S6. ANOVA table of the 3^2-experimental design. Significant effects are highlighted in bold. Table S7. Effects Estimate. Variables as coded variables of the 3^3-experimental design. Significant effects are highlighted in bold.

Author Contributions: Conceptualization, M.E.K.F.; methodology and investigation M.E.K.F.; J.L.D.d.T., L.S.R., L.F. and E.A.; validation M.E.K.F., G.G.L., O.A.A.d.S. and R.B.; writing—review and editing M.E.K.F., A.M.T. and G.G.L. All authors have read and agreed to the published version of the manuscript.

Funding: This research received no external funding.

Data Availability Statement: The data used to support the findings of this study are included within the article.

Acknowledgments: The authors thank the Capes, Fundação Araucaria, and CNPq agencies, analyzes performed at the laboratories LabMult C^2MMa—UTFPR—Ponta Grossa and LabMult CA—UTFPR—Pato Branco. Jose L. Diaz De Tuesta acknowledges the financial support through the

program of Atracción al Talento of Comunidad de Madrid (Spain) for the individual research grant 2022-T1/AMB-23946.

Conflicts of Interest: The authors declare no conflict of interest.

References

1. Boulkhessaim, S.; Gacem, A.; Khan, S.H.; Amari, A.; Yadav, V.K.; Harharah, H.N.; Elkhaleefa, A.M.; Yadav, K.K.; Rather, S.U.; Ahn, H.J.; et al. Emerging Trends in the Remediation of Persistent Organic Pollutants Using Nanomaterials and Related Processes: A Review. *Nanomaterials* **2022**, *12*, 2148. [CrossRef] [PubMed]
2. Aravind Kumar, J.; Krithiga, T.; Sathish, S.; Renita, A.A.; Prabu, D.; Lokesh, S.; Geetha, R.; Namasivayam, S.K.R.; Sillanpaa, M. Persistent Organic Pollutants in Water Resources: Fate, Occurrence, Characterization and Risk Analysis. *Sci. Total Environ.* **2022**, *831*, 154808. [CrossRef] [PubMed]
3. Abreu, E.; Fidelis, M.Z.; Fuziki, M.E.; Malikoski, R.M.; Mastsubara, M.C.; Imada, R.E.; Diaz de Tuesta, J.L.; Gomes, H.T.; Anziliero, M.D.; Baldykowski, B.; et al. Degradation of Emerging Contaminants: Effect of Thermal Treatment on Nb_2O_5 as Photocatalyst. *J. Photochem. Photobiol. A Chem.* **2021**, *419*, 113484. [CrossRef]
4. Gholamian, S.; Hamzehloo, M.; Farrokhnia, A. Enhanced Visible-Light Photocatalysis of TiO_2/Fe_3O_4/BiOI Nanocomposites as Magnetically Recoverable for the Degradation of Dye Pollutants. *J. Environ. Chem. Eng.* **2021**, *9*, 104937. [CrossRef]
5. Olea, M.A.U.; Bueno, J.D.J.P.; Pérez, A.X.M. Nanometric and Surface Properties of Semiconductors Correlated to Photocatalysis and Photoelectrocatalysis Applied to Organic Pollutants—A Review. *J. Environ. Chem. Eng.* **2021**, *9*, 106480. [CrossRef]
6. Rabani, I.; Tahir, M.S.; Afzal, F.; Truong, H.B.; Kim, M.; Seo, Y.S. High-Efficient Mineralization Performance of Photocatalysis Activity towards Organic Pollutants over Ruthenium Nanoparticles Stabilized by Metal Organic Framework. *J. Environ. Chem. Eng.* **2023**, *11*, 109235. [CrossRef]
7. Akpan, U.G.; Hameed, B.H. Parameters Affecting the Photocatalytic Degradation of Dyes Using TiO_2-Based Photocatalysts: A Review. *J. Hazard. Mater.* **2009**, *170*, 520–529. [CrossRef]
8. Al-Mamun, M.R.; Kader, S.; Islam, M.S.; Khan, M.Z.H. Photocatalytic Activity Improvement and Application of UV-TiO_2 Photocatalysis in Textile Wastewater Treatment: A Review. *J. Environ. Chem. Eng.* **2019**, *7*, 103248. [CrossRef]
9. Prado, A.G.S.; Bolzon, L.B.; Pedroso, C.P.; Moura, A.O.; Costa, L.L. Nb_2O_5 as Efficient and Recyclable Photocatalyst for Indigo Carmine Degradation. *Appl. Catal. B* **2008**, *82*, 219–224. [CrossRef]
10. Marques, R.R.N.; Sampaio, M.J.; Carrapiço, P.M.; Silva, C.G.; Morales-Torres, S.; Dražić, G.; Faria, J.L.; Silva, A.M.T. Photocatalytic Degradation of Caffeine: Developing Solutions for Emerging Pollutants. *Catal. Today* **2013**, *209*, 108–115. [CrossRef]
11. Chen, D.; Cheng, Y.; Zhou, N.; Chen, P.; Wang, Y.; Li, K.; Huo, S.; Cheng, P.; Peng, P.; Zhang, R.; et al. Photocatalytic Degradation of Organic Pollutants Using TiO_2-Based Photocatalysts: A Review. *J. Clean. Prod.* **2020**, *268*, 121725. [CrossRef]
12. Hashimoto, K.; Irie, H.; Fujishima, A. TiO_2 Photocatalysis: A Historical Overview and Future Prospects. *Jpn. J. Appl. Phys.* **2005**, *44*, 8269–8285. [CrossRef]
13. Raba, A.M.; Bautista-Ruíz, J.; Joya, M.R. Synthesis and Structural Properties of Niobium Pentoxide Powders: A Comparative Study of the Growth Process. *Mater. Res.* **2016**, *19*, 1381–1387. [CrossRef]
14. Zhao, Y.; Eley, C.; Hu, J.; Foord, J.S.; Ye, L.; He, H.; Tsang, S.C.E. Shape-Dependent Acidity and Photocatalytic Activity of Nb_2O_5 Nanocrystals with an Active TT (001) Surface. *Angew. Chem. Int. Ed.* **2012**, *51*, 3846–3849. [CrossRef] [PubMed]
15. Castro, D.C.; Cavalcante, R.P.; Jorge, J.; Martines, M.A.U.; Oliveira, L.C.S.; Casagrande, G.A.; Machulek, A. Synthesis and Characterization of Mesoporous Nb_2O_5 and Its Application for Photocatalytic Degradation of the Herbicide Methylviologen. *J. Braz. Chem. Soc.* **2016**, *27*, 303–313. [CrossRef]
16. Sacco, O.; Murcia, J.J.; Lara, A.E.; Hernández-Laverde, M.; Rojas, H.; Navío, J.A.; Hidalgo, M.C.; Vaiano, V. Pt–TiO_2–Nb_2O_5 Heterojunction as Effective Photocatalyst for the Degradation of Diclofenac and Ketoprofen. *Mater. Sci. Semicond. Process* **2020**, *107*, 104839. [CrossRef]
17. Rafael, R.A.; Noronha, F.B.; Gaspar, A.B. Synthesis and Characterization of Ti-Nb_2O_5 Catalysts for Discoloration Reaction of Bromophenol Blue and Indigo Carmine Dyes. *Top. Catal.* **2020**, *63*, 1066–1076. [CrossRef]
18. De Andrade, F.V.; De Lima, G.M.; Augusti, R.; Coelho, M.G.; Assis, Y.P.Q.; Machado, I.R.M. A New Material Consisting of TiO_2 Supported on Nb_2O_5 as Photocatalyst for the Degradation of Organic Contaminants in Aqueous Medium. *J. Environ. Chem. Eng.* **2014**, *2*, 2352–2358. [CrossRef]
19. López, A.L.B.; Castro, I.M. Niobium-Titanium-Based Photocatalysts: Its Potentials for Free Cyanide Oxidation in Residual Aqueous Effluent. *Front. Chem.* **2020**, *8*, 499621. [CrossRef]
20. Topare, N.S.; Raut, S.J.; Khedkar, S.V.; Renge, V.C. A Study of Process Variables for the Photocatalytic Degradation of Rhodamine-B Using TiO_2 and Nb_2O_5. *J. Indian. Chem. Soc.* **2013**, *90*, 2193–2198.
21. Fontana, K.B.K.B.; Chaves, E.S.E.S.; Kosera, V.S.V.S.; Lenzi, G.G.G.G. Barium Removal by Photocatalytic Process: An Alternative for Water Treatment. *J. Water Process Eng.* **2018**, *22*, 163–171. [CrossRef]
22. Cui, H.; Dwight, K.; Soled, S.; Wold, A. Surface Acidity and Photocatalytic Activity of Nb_2O_5/TiO_2 Photocatalysts. *J. Solid. State Chem.* **1995**, *115*, 187–191. [CrossRef]

23. Ferraz, N.P.; Marcos, F.C.F.; Nogueira, A.E.; Martins, A.S.; Lanza, M.R.V.; Assaf, E.M.; Asencios, Y.J.O. Hexagonal-Nb_2O_5/Anatase-TiO_2 Mixtures and Their Applications in the Removal of Methylene Blue Dye under Various Conditions. *Mater. Chem. Phys.* **2017**, *198*, 331–340. [CrossRef]
24. Yan, J.; Wu, G.; Guan, N.; Li, L. Nb_2O_5/TiO_2 Heterojunctions: Synthesis Strategy and Photocatalytic Activity. *Appl. Catal. B* **2014**, *152–153*, 280–288. [CrossRef]
25. Ferrari-Lima, A.M.; Marques, R.G.; Gimenes, M.L.; Fernandes-Machado, N.R.C. Synthesis, Characterisation and Photocatalytic Activity of N-Doped TiO2-Nb2O5 Mixed Oxides. *Catal. Today* **2015**, *254*, 119–128. [CrossRef]
26. Sedneva, T.A.; Lokshin, E.P.; Belikov, M.L.; Belyaevskii, A.T. TiO_2- and Nb_2O_5-Based Photocatalytic Composites. *Inorg. Mater.* **2013**, *49*, 382–389. [CrossRef]
27. Bi, X.; Du, G.; Kalam, A.; Sun, D.; Zhao, W.; Yu, Y.; Su, Q.; Xu, B.; Al-Sehemi, A.G. Constructing Anatase TiO_2/Amorphous Nb_2O_5 Heterostructures to Enhance Photocatalytic Degradation of Acetaminophen and Nitrogen Oxide. *J. Colloid. Interface Sci.* **2021**, *601*, 346–354. [CrossRef]
28. Shiraishi, Y.; Imai, J.; Yasumoto, N.; Sakamoto, H.; Tanaka, S.; Ichikawa, S.; Hirai, T. Doping of Nb5+ Species at the Au-TiO_2 Interface for Plasmonic Photocatalysis Enhancement. *Langmuir* **2019**, *35*, 5455–5462. [CrossRef]
29. Ücker, C.L.; Riemke, F.; Goetzke, V.; Moreira, M.L.; Raubach, C.W.; Longo, E.; Cava, S. Facile Preparation of Nb_2O_5/TiO_2 Heterostructures for Photocatalytic Application. *Chem. Phys. Impact* **2022**, *4*, 100079. [CrossRef]
30. Ahmad, A.; Shah, J.A.; Buzby, S.; Shah, S.I. Structural Effects of Codoping of Nb and Sc in Titanium Dioxide Nanoparticles. *Eur. J. Inorg. Chem.* **2008**, *2008*, 948–953. [CrossRef]
31. Brahimi, R.; Bessekhouad, Y.; Bouguelia, A.; Trari, M. $CuAlO_2$/TiO_2 Heterojunction Applied to Visible Light H_2 Production. *J. Photochem. Photobiol. A Chem.* **2007**, *186*, 242–247. [CrossRef]
32. Xu, Y.; Schoonen, M.A.A. The Absolute Energy Positions of Conduction and Valence Bands of Selected Semiconducting Minerals. *Am. Mineral.* **2000**, *85*, 543–556. [CrossRef]
33. Gondal, M.A.; Sayeed, M.N.; Seddigi, Z. Laser Enhanced Photocatalytic Removal of Phenol from Water Using p-Type NiO Semiconductor Catalyst. *J. Hazard. Mater.* **2008**, *155*, 83–89. [CrossRef]
34. Ratola, N.; Cincinelli, A.; Alves, A.; Katsoyiannis, A. Occurrence of Organic Microcontaminants in the Wastewater Treatment Process. A Mini Review. *J. Hazard. Mater.* **2012**, *239–240*, 1–18. [CrossRef]
35. Nikolopoulou, V.; Ajibola, A.S.; Aalizadeh, R.; Thomaidis, N.S. Wide-Scope Target and Suspect Screening of Emerging Contaminants in Sewage Sludge from Nigerian WWTPs by UPLC-QToF-MS. *Sci. Total Environ.* **2023**, *857*, 159529. [CrossRef] [PubMed]
36. Vione, D.; Picatonotto, T.; Carlotti, M.E. Photodegradation of Phenol and Salicylic Acid by Coated Rutile-Based Pigments: A New Approach for the Assessment of Sunscreen Treatment Efficiency. *J. Cosmet. Sci.* **2003**, *54*, 513–524. [PubMed]
37. Bertinetti, S.; Minella, M.; Barsotti, F.; Maurino, V.; Minero, C.; Özensoy, E.; Vione, D. A Methodology to Discriminate between Hydroxyl Radical-Induced Processes and Direct Charge-Transfer Reactions in Heterogeneous Photocatalysis. *J. Adv. Oxid. Technol.* **2016**, *19*, 236–245. [CrossRef]
38. Chhor, K.; Bocquet, J.F.; Colbeau-Justin, C. Comparative Studies of Phenol and Salicylic Acid Photocatalytic Degradation: Influence of Adsorbed Oxygen. *Mater. Chem. Phys.* **2004**, *86*, 123–131. [CrossRef]
39. Barbero, N.; Vione, D. Why Dyes Should Not Be Used to Test the Photocatalytic Activity of Semiconductor Oxides. *Environ. Sci. Technol.* **2016**, *50*, 2130–2131. [CrossRef]
40. Karimi, F.; Rezaei-savadkouhi, N.; Uçar, M.; Aygun, A.; Elhouda Tiri, R.N.; Meydan, I.; Aghapour, E.; Seckin, H.; Berikten, D.; Gur, T.; et al. Efficient Green Photocatalyst of Silver-Based Palladium Nanoparticles for Methyle Orange Photodegradation, Investigation of Lipid Peroxidation Inhibition, Antimicrobial, and Antioxidant Activity. *Food Chem. Toxicol.* **2022**, *169*, 113406. [CrossRef]
41. Sinha, T.; Ahmaruzzaman, M.; Adhikari, P.P.; Bora, R. Green and Environmentally Sustainable Fabrication of Ag-SnO_2 Nanocomposite and Its Multifunctional Efficacy as Photocatalyst and Antibacterial and Antioxidant Agent. *ACS Sustain. Chem. Eng.* **2017**, *5*, 4645–4655. [CrossRef]
42. Eskikaya, O.; Ozdemir, S.; Tollu, G.; Dizge, N.; Ramaraj, R.; Manivannan, A.; Balakrishnan, D. Synthesis of Two Different Zinc Oxide Nanoflowers and Comparison of Antioxidant and Photocatalytic Activity. *Chemosphere* **2022**, *306*, 135389. [CrossRef] [PubMed]
43. Muthuvel, A.; Said, N.M.; Jothibas, M.; Gurushankar, K.; Mohana, V. Microwave-Assisted Green Synthesis of Nanoscaled Titanium Oxide: Photocatalyst, Antibacterial and Antioxidant Properties. *J. Mater. Sci. Mater. Electron.* **2021**, *32*, 23522–23539. [CrossRef]
44. Hwang, K.J.; Lee, J.W.; Shim, W.G.; Jang, H.D.; Lee, S.I.; Yoo, S.J. Adsorption and Photocatalysis of Nanocrystalline TiO_2 Particles Prepared by Sol-Gel Method for Methylene Blue Degradation. *Adv. Powder Technol.* **2012**, *23*, 414–418. [CrossRef]
45. Yukselen, Y.; Kaya, A. Suitability of the Methylene Blue Test for Surface Area, Cation Exchange Capacity and Swell Potential Determination of Clayey Soils. *Eng. Geol.* **2008**, *102*, 38–45. [CrossRef]
46. Yener, N.; Bier, C.; Önal, M.; Sarikaya, Y. Simultaneous Determination of Cation Exchange Capacity and Surface Area of Acid Activated Bentonite Powders by Methylene Blue Sorption. *Appl. Surf. Sci.* **2012**, *258*, 2534–2539. [CrossRef]
47. Gürses, A.; Karaca, S.; Doğar, Ç.; Bayrak, R.; Açikyildiz, M.; Yalçin, M. Determination of Adsorptive Properties of Clay/Water System: Methylene Blue Sorption. *J. Colloid. Interface Sci.* **2004**, *269*, 310–314. [CrossRef]

48. da Silva, A.L.; Hotza, D.; Castro, R.H.R.R. Surface Energy Effects on the Stability of Anatase and Rutile Nanocrystals: A Predictive Diagram for Nb_2O_5-Doped-TiO_2. *Appl. Surf. Sci.* **2017**, *393*, 103–109. [CrossRef]
49. Da Silva, A.L.; Muche, D.N.F.; Dey, S.; Hotza, D.; Castro, R.H.R. Photocatalytic Nb_2O_5-Doped TiO_2 Nanoparticles for Glazed Ceramic Tiles. *Ceram. Int.* **2016**, *42*, 5113–5122. [CrossRef]
50. Kumari, N.; Gaurav, K.; Samdarshi, S.K.; Bhattacharyya, A.S.; Paul, S.; Rajbongshi, B.M.; Mohanty, K. Dependence of Photoactivity of Niobium Pentoxide (Nb_2O_5) on Crystalline Phase and Electrokinetic Potential of the Hydrocolloid. *Sol. Energy Mater. Sol. Cells* **2020**, *208*, 110408. [CrossRef]
51. Atanacio, A.J.; Bak, T.; Nowotny, J. Niobium Segregation in Niobium-Doped Titanium Dioxide (Rutile). *J. Phys. Chem. C* **2014**, *118*, 11174–11185. [CrossRef]
52. Vaizoğullar, A.İ. Ternary CdS/MoS_2/ZnO Photocatalyst: Synthesis, Characterization and Degradation of Ofloxacin Under Visible Light Irradiation. *J. Inorg. Organomet. Polym. Mater.* **2020**, *30*, 4129–4141. [CrossRef]
53. Rahman, M.M.; Muttakin, M.; Pal, A.; Shafiullah, A.Z.; Saha, B.B. A Statistical Approach to Determine Optimal Models for IUPAC-Classified Adsorption Isotherms. *Energies* **2019**, *12*, 4565. [CrossRef]
54. Yurdakal, S.; Garlisi, C.; Özcan, L.; Bellardita, M.; Palmisano, G. (Photo)Catalyst Characterization Techniques: Adsorption Isotherms and BET, SEM, FTIR, UV-Vis, Photoluminescence, and Electrochemical Characterizations. In *Heterogeneous Photocatalysis: Relationships with Heterogeneous Catalysis and Perspectives*; Elsevier: Amsterdam, The Netherlands, 2019; pp. 87–152. ISBN 9780444640154.
55. Gomes, G.H.M.; Mohallem, N.D.S. Insights into the TT-Nb_2O_5 Crystal Structure Behavior. *Mater. Lett.* **2022**, *318*, 132136. [CrossRef]
56. Maver, K.; Arčon, I.; Fanetti, M.; Emin, S.; Valant, M.; Lavrenčič Štangar, U. Improved Photocatalytic Activity of Anatase-Rutile Nanocomposites Induced by Low-Temperature Sol-Gel Sn-Modification of TiO_2. *Catal. Today* **2021**, *361*, 124–129. [CrossRef]
57. Souza, R.P.; Ambrosio, E.; Souza, M.T.F.; Freitas, T.K.F.S.; Ferrari-Lima, A.M.; Garcia, J.C. Solar Photocatalytic Degradation of Textile Effluent with TiO_2, ZnO, and Nb_2O_5 Catalysts: Assessment of Photocatalytic Activity and Mineralization. *Environ. Sci. Pollut. Res.* **2017**, *24*, 12691–12699. [CrossRef]
58. Hu, R.; Zhang, L.; Hu, J. Study on the Kinetics and Transformation Products of Salicylic Acid in Water via Ozonation. *Chemosphere* **2016**, *153*, 394–404. [CrossRef]
59. Fuziki, M.E.K.; Ribas, L.S.; Tusset, A.M.; Brackmann, R.; Dos Santos, O.A.A.; Lenzi, G.G. Pharmaceutical Compounds Photolysis: PH Influence. *Heliyon* **2023**, *9*, e13678. [CrossRef]
60. Lu, J.; Jin, H.; Dai, Y.; Yang, K.; Huang, B. Effect of Electronegativity and Charge Balance on the Visible-Light- Responsive Photocatalytic Activity of Nonmetal Doped Anatase TiO_2. *Int. J. Photoenergy* **2012**, *2012*, 928503. [CrossRef]
61. Parr, R.G.; Pearson, R.G. *Absolute Hardness: Companion Parameter to Absolute Electronegativity*; ACS Publications: Washington, DC, USA, 1983; Volume 105.
62. Xian, T.; Yang, H.; Di, L.J.; Dai, J.F. Enhanced Photocatalytic Activity of $BaTiO_3$@g-C_3N_4 for the Degradation of Methyl Orange under Simulated Sunlight Irradiation. *J. Alloys Compd.* **2015**, *622*, 1098–1104. [CrossRef]
63. Chang, C.Y.; Hsieh, Y.H.; Hsieh, L.L.; Yao, K.S.; Cheng, T.C. Establishment of Activity Indicator of TiO_2 Photocatalytic Reaction-Hydroxyl Radical Trapping Method. *J. Hazard. Mater.* **2009**, *166*, 897–903. [CrossRef] [PubMed]
64. Vamathevan, V.; Amal, R.; Beydoun, D.; Low, G.; Mcevoy, S. Photocatalytic Oxidation of Organics in Water Using Pure and Silver-Modified Titanium Dioxide Particles. *J. Photochem. Photobiol. A Chem.* **2002**, *148*, 233–245. [CrossRef]
65. Bracco, E.; Butler, M.; Carnelli, P.; Candal, R. TiO_2 and N-TiO_2-Photocatalytic Degradation of Salicylic Acid in Water: Characterization of Transformation Products by Mass Spectrometry. *Environ. Sci. Pollut. Res.* **2020**, *27*, 28469–28479. [CrossRef] [PubMed]
66. Zupanc, M.; Petkovšek, M.; Zevnik, J.; Kozmus, G.; Šmid, A.; Dular, M. Anomalies Detected during Hydrodynamic Cavitation When Using Salicylic Acid Dosimetry to Measure Radical Production. *Chem. Eng. J.* **2020**, *396*, 125389. [CrossRef]
67. Plavac, B.; Grčić, I.; Brnardić, I.; Grozdanić, V.; Papić, S. Kinetic Study of Salicylic Acid Photocatalytic Degradation Using Sol–Gel Anatase Thin Film with Enhanced Long-Term Activity. *React. Kinet. Mech. Catal.* **2017**, *120*, 385–401. [CrossRef]
68. Leite dos Santos, A.; Almeida Dias, J.; Tiago dos Santos Tavares, G.; Romito de Mendonça, V.; Giraldi, T.R. Niobium Pentoxide as an Adsorbent for Methylene Blue Removal: Synthesis, Characterization and Thermal Stability. *Mater. Chem. Phys.* **2023**, *301*, 127659. [CrossRef]
69. Tamura, H.; Mita, K.; Tanaka, A.; Ito, M. Mechanism of Hydroxylation of Metal Oxide Surfaces. *J. Colloid. Interface Sci.* **2001**, *243*, 202–207. [CrossRef]
70. Chu, L.; Liu, W.; Yu, A.; Qin, Z.; Hu, R.; Shu, H.; Luo, Q.P.; Min, Y.; Yang, J.; Li, X. Effect of TiO_2 Modification on Urchin-like Orthorhombic Nb_2O_5 Nanospheres as Photoelectrodes in Dye-Sensitized Solar Cells. *Solar Energy* **2017**, *153*, 584–589. [CrossRef]
71. Oliveira, I.R.; Barbosa, A.M.; Santos, K.W.; Lança, M.C.; Lima, M.M.R.A.; Vieira, T.; Silva, J.C.; Borges, J.P. Properties of Strontium-Containing BG 58S Produced by Alkali-Mediated Sol-Gel Process. *Ceram. Int.* **2022**, *48*, 11456–11465. [CrossRef]
72. Khalil, K.M.S.; Zaki, M.I. Synthesis of High Surface Area Titania Powders via Basic Hydrolysis of Titanium(IV) Isopropoxide. *Powder Technol.* **1997**, *92*, 233–239. [CrossRef]
73. Ghoreishian, S.M.; Seeta Rama Raju, G.; Pavitra, E.; Kwak, C.H.; Han, Y.K.; Huh, Y.S. Controlled Synthesis of Hierarchical α-Nickel Molybdate with Enhanced Solar-Light-Responsive Photocatalytic Activity: A Comprehensive Study on the Kinetics and Effect of Operational Factors. *Ceram. Int.* **2019**, *45*, 12041–12052. [CrossRef]

74. Szekeres, M.; Tombácz, E. Surface Charge Characterization of Metal Oxides by Potentiometric Acid-Base Titration, Revisited Theory and Experiment. *Colloids Surf. A Physicochem. Eng. Asp.* **2012**, *414*, 302–313. [CrossRef]
75. Fuziki, M.E.K.; Brackmann, R.; Dias, D.T.; Tusset, A.M.; Specchia, S.; Lenzi, G.G. Effects of Synthesis Parameters on the Properties and Photocatalytic Activity of the Magnetic Catalyst $TiO_2/CoFe_2O_4$ Applied to Selenium Photoreduction. *J. Water Process Eng.* **2021**, *42*, 102163. [CrossRef]
76. Makuła, P.; Pacia, M.; Macyk, W. How To Correctly Determine the Band Gap Energy of Modified Semiconductor Photocatalysts Based on UV-Vis Spectra. *J. Phys. Chem. Lett.* **2018**, *9*, 6814–6817. [CrossRef] [PubMed]
77. Gervasi, S.; Blangetti, N.; Freyria, F.S.; Guastella, S.; Bonelli, B. Undoped and Fe-Doped Anatase/Brookite TiO_2 Mixed Phases, Obtained by a Simple Template-Free Synthesis Method: Physico-Chemical Characterization and Photocatalytic Activity towards Simazine Degradation. *Catalysts* **2023**, *13*, 667. [CrossRef]
78. Shenoy, S.; Farahat, M.M.; Chuaicham, C.; Sekar, K.; Ramasamy, B.; Sasaki, K. Mixed-Phase Fe_2O_3 Derived from Natural Hematite Ores/C3N4 Z-Scheme Photocatalyst for Ofloxacin Removal. *Catalysts* **2023**, *13*, 792. [CrossRef]
79. Zangeneh, H.; Mousavi, S.A.; Eskandari, P.; Amarloo, E.; Farghelitiyan, J.; Mohammadi, S. Comparative Study on Photocatalytic Performance of TiO_2 Doped with Different Amino Acids in Degradation of Antibiotics. *Water* **2023**, *15*, 535. [CrossRef]
80. Li, X.; Wan, T.; Qiu, J.; Wei, H.; Qin, F.; Wang, Y.; Liao, Y.; Huang, Z.; Tan, X. In-Situ Photocalorimetry-Fluorescence Spectroscopy Studies of RhB Photocatalysis over Z-Scheme g-C_3N_4@Ag@Ag_3PO_4Nanocomposites: A Pseudo-Zero-Order Rather than a First-Order Process. *Appl. Catal. B* **2017**, *217*, 591–602. [CrossRef]
81. Wang, Y.; Zhang, Y.; Zhang, T.C.; Xiang, G.; Wang, X.; Yuan, S. Removal of Trace Arsenite through Simultaneous Photocatalytic Oxidation and Adsorption by Magnetic Fe_3O_4@PpPDA@TiO_2Core-Shell Nanoparticles. *ACS Appl. Nano Mater.* **2020**, *3*, 8495–8504. [CrossRef]
82. Ghaffar, S.; Abbas, A.; Naeem-ul-Hassan, M.; Assad, N.; Sher, M.; Ullah, S.; Alhazmi, H.A.; Najmi, A.; Zoghebi, K.; Al Bratty, M.; et al. Improved Photocatalytic and Antioxidant Activity of Olive Fruit Extract-Mediated ZnO Nanoparticles. *Antioxidants* **2023**, *12*, 1201. [CrossRef]
83. Nawaz, M.; Almofty, S.A.; Qureshi, F. Preparation, Formation Mechanism, Photocatalytic, Cytotoxicity and Antioxidant Activity of Sodium Niobate Nanocubes. *PLoS ONE* **2018**, *13*, e0204061. [CrossRef] [PubMed]